



19 **Abstract**

20 Spermatozoa are attracted to their conspecific female gamete by diffusive molecules  
21 released from the egg investments, a process called chemotaxis. The decapeptide  
22 speract induces metabolic and permeability changes in *Strongylocentrotus purpuratus*  
23 sea urchin sperm. In spite of decades since speract purification from *S. purpuratus* egg  
24 investments, sperm chemotaxis has not been demonstrated in this species. By studying  
25 how the stimulus function, which spermatozoa experience during the accumulation of  
26 bound chemoattractants throughout their trajectory, influences both their motility  
27 response and their internal  $\text{Ca}^{2+}$  oscillations, we were able to show, for the first time,  
28 that *S. purpuratus* spermatozoa exhibit chemotaxis under sufficiently steep speract  
29 concentration gradients. We demonstrate that this process arises through frequency  
30 entrainment of the coupled metabolic oscillators.

## 31 **Introduction**

32 Broadcast spawning organisms, such as marine invertebrates, release their gametes  
33 into open sea, where they are often subject to extensive dilution that reduces the  
34 probability of gamete encounter (Lotterhos, 2010). In many marine organisms, female  
35 gametes release diffusible molecules that attract homologous spermatozoa (Lillie, 1913,  
36 Miller, 1985, Suzuki, 1995). Propelled by their beating flagella, spermatozoa detect and  
37 respond to chemoattractant concentration gradients by steering their swimming  
38 trajectory toward the gradient source: the egg. Though it was in bracken ferns where  
39 sperm chemotaxis was first identified (Pfeffer, 1884), sea urchins are currently the best-  
40 characterized model system for studying sperm chemotaxis at a molecular level  
41 (Alvarez et al., 2012, Cook et al., 1994, Darszon et al., 2008, Strunker et al., 2015,  
42 Wood et al., 2015).

43 The sea urchin egg is surrounded by an extracellular matrix which contains short  
44 sperm-activating peptides (SAPs), that modulate sperm motility through altering  
45 intracellular  $\text{Ca}^{2+}$  concentration ( $[\text{Ca}^{2+}]_i$ ) and other signaling intermediates (Darszon et  
46 al., 2008, Suzuki, 1995). The probability of sperm-egg encounter is enhanced by the  
47 prompt transduction of the biochemical signals triggered by SAPs into the appropriate  
48 reorientation of the sperm trajectory.

49 The decapeptide speract is one of best characterized members of the SAP family due  
50 to its powerful stimulating effect on metabolism, permeability and motility in *S.*  
51 *purpuratus* and *L. pictus* spermatozoa. In 2003, it was shown that the binding of speract  
52 to its receptor located in the flagellar plasma membrane, triggers a train of  $[\text{Ca}^{2+}]_i$   
53 increases in immobilized *S. purpuratus* spermatozoa (Wood et al., 2003). This calcium  
54 signal was thought to regulate the activity of dynein motor proteins in the flagellum,  
55 thus might modulate the swimming path of sperm (Brokaw, 1979).

56 A direct link between  $[Ca^{2+}]_i$  signaling and sperm motility was established through  
57 the use of optochemical techniques to rapidly, and non-turbulently, expose swimming  
58 sea urchin spermatozoa to their conspecific attractant in a well-controlled experimental  
59 regime (Wood et al., 2005, Bohmer et al., 2005). Currently, it is well established that  
60 the transient  $[Ca^{2+}]_i$  increases triggered by chemoattractants produce a sequence of turns  
61 and straight swimming episodes (turn-and-run), where each turning event results from  
62 the rapid increase in the  $[Ca^{2+}]_i$  (Wood et al., 2005, Bohmer et al., 2005, Shiba et al.,  
63 2008, Alvarez et al., 2012). The turn-and-run seems to be a general requirement for  
64 sperm chemotaxis, however it is not sufficient on its own to produce a chemotactic  
65 response (Guerrero et al., 2010a, Strunker et al., 2015, Wood et al., 2007, Wood et al.,  
66 2005).

67

68 Our current understanding of chemotaxis, suggests that sperm first sample the  
69 chemoattractant concentration gradient by swimming in periodic paths (either circular  
70 2D or helical 3D). During the sampling phase, the accumulation of bound  
71 chemoattractants triggers  $[Ca^{2+}]_i$  transients that control the waveform of the flagellar  
72 beat. In this way, the alternate periods of asymmetrical (turn) and symmetrical (run)  
73 flagellar beating give rise to a looping swimming pattern that guides up to the source of  
74 the chemoattractant gradient.

75 Friedrich and Jülicher proposed a generic theory that captures the essence of sperm  
76 navigation following periodic paths in a non-homogeneous chemoattractant field, where  
77 the sampling of a periodic concentration stimulus  $s(t)$  is translated by intracellular  
78 signaling  $i(t)$  into the periodic modulation of the swimming path curvature  $k(t)$   
79 (Friedrich and Jülicher, 2007, Friedrich and Jülicher, 2008). As result, the periodic  
80 swimming path drifts in a direction that depends on the internal dynamics of the

81 signaling system. In this theory, the latency of the intracellular signaling (the  $[Ca^{2+}]_i$   
82 signal), expressed as the phase shift between  $s(t)$  and  $k(t)$ , is a crucial determinant of the  
83 directed looping of the swimming trajectory up the chemical concentration field. This  
84 theory also predicts that chemotaxis is a robust property of the system that does not  
85 require fine-tuning of parameters (if the signaling system is adaptive) (Friedrich and  
86 Jülicher, 2008, Friedrich and Jülicher, 2009). In other words, there is a large range of  
87 parameters for which sperm chemotaxis is a robust outcome, providing an effective way  
88 for sampling the local chemoattractant concentration field and detecting the direction of  
89 the concentration gradient (Kaupp et al., 2003, Kashikar et al., 2012, Pichlo et al., 2014,  
90 Friedrich and Jülicher, 2008, Friedrich and Jülicher, 2007).

91 Even though the conceptual framework of Friedrich & Jülicher provides insights into  
92 the mechanism governing sperm chemotaxis, it does not explore the scenario whereby  
93 chemoattractants trigger an autonomous  $[Ca^{2+}]_i$  oscillator operating in the absence of a  
94 periodic stimulus. The existence of an autonomous  $[Ca^{2+}]_i$  oscillator triggered by  
95 chemoattractants (Wood et al., 2003, Espinal et al., 2011, Aguilera et al., 2012) suggests  
96 that sperm chemotaxis might operate in a dynamical space where two autonomous  
97 oscillators, namely the stimulus function and the internal  $Ca^{2+}$  oscillator, reach  
98 frequency entrainment (Pikovsky et al., 2001).

99 In spite of 30 years of research since speract's isolation from *S. purpuratus* oocytes  
100 (Hansbrough and Garbers, 1981, Suzuki, 1995), chemotaxis of *S. purpuratus* sperm  
101 towards this peptide has not yet been demonstrated (Cook et al., 1994, Darszon et al.,  
102 2008, Guerrero et al., 2010b, Kaupp, 2012, Miller, 1985, Wood et al., 2015). A  
103 comparison between individual *L. pictus* and *S. purpuratus* sperm responses to a  
104 specific chemoattractant concentration gradient generated by photoactivating caged  
105 speract (CS) revealed that only *L. pictus* spermatozoa exhibit chemotaxis under these

106 conditions (Guerrero et al., 2010a). In that study, *L. pictus* spermatozoa experience  
107  $[Ca^{2+}]_i$  fluctuations and pronounced turns while swimming in descending speract  
108 gradients, that result in spermatozoa reorienting their swimming behavior along the  
109 positive chemoattractant concentration gradient. In contrast, *S. purpuratus* spermatozoa  
110 experience similar trains of  $[Ca^{2+}]_i$  fluctuations that in turn drive them to relocate, but  
111 with no preference towards the center of the chemoattractant gradient (Guerrero et al.,  
112 2010a).

113 The precise triggering of  $[Ca^{2+}]_i$  fluctuations associated to sperm turning events  
114 towards the chemoattractant gradient, as well as the turn-and-run behavior seem to be  
115 general requirements for sperm chemotaxis in marine invertebrates (Bohmer et al.,  
116 2005, Guerrero et al., 2010a, Jikeli et al., 2015, Kashikar et al., 2012, Shiba et al., 2008,  
117 Strunker et al., 2015, Wood et al., 2015), and could be important features of sperm  
118 chemotaxis in general.

119 In the present work, we investigate whether *S. purpuratus* spermatozoa can undergo  
120 chemotaxis. Particularly, we examined whether there is a physical limit to the sampling  
121 of the chemoattractant concentration gradient needed for detection that has, to date,  
122 prevented observation and characterization of their chemotactic response. We report  
123 that *S. purpuratus* spermatozoa are chemotactic only when exposed to much steeper  
124 speract concentration gradients than those previously employed. Furthermore, we  
125 explored the coupling between the recruitment of speract molecules during the sperm  
126 voyage, the triggered signaling cascade and the internal  $Ca^{2+}$  oscillator; and demonstrate  
127 that sperm chemotaxis arises through coupled metabolic oscillators.

## 128 **Results**

129 Chemotaxis refers to the directed movement of an organism or a cell in a chemical  
130 gradient. The first step in a chemotactic response is the sampling of a chemoattractant  
131 field, from where in a given time  $T$ , statistical fluctuations limit the precision with  
132 which the searcher can determine the concentration of the chemoattractant (Berg and  
133 Purcell, 1977, Vergassola et al., 2007, Dusenbery, 2011).

134 Assuming that the number of ligands that collide with a single receptor per unit of  
135 time is proportional to radius of the receptor  $s$ , the concentration of the attractant  $c$  and  
136 the diffusion constant of the attractant  $D$ , the total number of collisions between  $N_R$   
137 receptors in a time interval  $T$  is  $x = N_R s D c T$ . The statistical fluctuation on the number  
138 of ligand-receptor collisions  $x$  follows a Poisson distribution, and therefore the expected  
139 value  $E[x]$  and the variance  $Var[x]$  are the same. In this scenario, the coefficient of  
140 variation is  $\frac{SD[x]}{E[x]} = \frac{\sqrt{Var[x]}}{E[x]} = \frac{\sqrt{E[x]}}{E[x]}$ . This coefficient can be interpreted as the smallest  
141 fractional error attainable in the determination of the concentration of the attractant (see  
142 **Theory** section) (Berg and Purcell, 1977, Dusenbery, 2011, Vergassola et al., 2007).

$$143 \quad u_1 = (N_R s D c T)^{-1/2} \quad (1)$$

144

### 145 *Uncertainty in the determination of the presence of chemoattractant molecules*

146 The flagella of sea urchin spermatozoa possess a large number of high affinity SAP  
147 receptors ( $10^4$ - $10^6$  depending on species and author) (Nishigaki and Darszon, 2000,  
148 Shimomura and Garbers, 1986, Smith and Garbers, 1982, Kaupp et al., 2008). This  
149 great number of SAP receptors provides spermatozoa with a fine-tuned sensory system  
150 able to respond to a wide range of SAP concentrations ( $10^{-12}$ - $10^{-6}$  M). That these  
151 receptors are distributed along the entire flagellum increases the probability of capturing  
152 even a few arriving molecules (Kaupp et al., 2003, Kashikar et al., 2012).

153 To understand the theoretical sampling capabilities of sea urchin spermatozoa, given  
154 a specific speract concentration (in a homogeneous concentration field), and flagellar  
155 receptor availability, we first computed the smallest fractional error attainable in the  
156 detection of a chemoattractant  $u_I$  at different concentrations, considering distinct  
157 receptor numbers. A theoretical *S. purpuratus* spermatozoon possessing  $N_R = 2 \times 10^4$   
158 receptors, will sample a medium containing 10 nM of speract in time  $T = 0.5$  s with an  
159 uncertainty of  $u_I = 0.006$  (**Figure 1 – figure supplement 1a** and **Figure 1 – table**  
160 **supplement 1**). Here, the time scale  $T$  was considered as the time needed for a *S.*  
161 *purpuratus* spermatozoon to traverse a distance equivalent to approximately half a  
162 circumference of its circular trajectory when confined to the water-glass boundary, in a  
163 homogeneous field of speract. The least fractional error attainable in the determination  
164 of the concentration of the attractant has no upper boundary, however  $u_I$  values greater  
165 than 1 indicates that stochastic fluctuations dominate over the signal (Berg and Purcell,  
166 1977). For simplicity,  $u_I$  was considered to operate in the range [0, 1]. In other words,  
167 our model spermatozoon, when exposed to a chemoattractant concentration of 10 nM,  
168 will be able to determine the presence of speract molecules with 0.6% of uncertainty in  
169 0.5 s.

170 If the spermatozoon finds itself in a sampling space of 1 pM of speract, this level of  
171 uncertainty increases to 60% over the same interval. It is likely that at speract  
172 concentrations below picomolar, an *S. purpuratus* spermatozoon will require relatively  
173 extended sampling times to determine the presence of speract molecules. For example,  
174 for a spermatozoon sampling a 1 pM concentration field of speract for 60 seconds, the  
175 uncertainty of receptor occupancy drops to 6% (**Figure 1 – figure supplement 1b**).

176 An important difference between *S. purpuratus* and *L. pictus* spermatozoa is their  
177 respective receptor density; the former possesses 3.15x fewer receptors than the latter (2

178  $\times 10^4$  versus  $6.3 \times 10^4$  receptors per cell, respectively) (**Figure 1 – table supplement 1**)  
179 (Nishigaki and Darszon, 2000, Nishigaki et al., 2001). Note that if *S. purpuratus*  
180 spermatozoa were to possess a receptor density equivalent to *L. pictus*, they would be  
181 able to sample a speract concentration field of 1 pM within 0.5 seconds with an  
182 uncertainty of  $u_1 = 0.4$  (40%) (**Figure 1 – figure supplement 1a**). Given the differences  
183 in sensitivities between these two species, the lack of chemotactic responses in *S.*  
184 *purpuratus* spermatozoa could possibly be explained, at least partially, by their lesser  
185 density of speract receptors, compared to *L. pictus*.

186

187 ***Uncertainty in the determination of sperm position in a non-homogeneous***  
188 ***chemoattractant concentration field***

189 To detect a chemoattractant concentration gradient, the signal at two given points,  
190 sampled throughout a time interval must be greater than the noise, which in this case  
191 would arise from spontaneous stochastic activation of one or more components of the  
192 chemoattractant signaling pathway (**Figure 1a**) (Berg and Purcell, 1977, Vergassola et  
193 al., 2007, Wood et al., 2015, Dusenbery, 2011). Information regarding the direction of  
194 the chemoattractant gradient results from the magnitude difference of the signal at two  
195 sampled positions (for further explanation see **Theory** section). The smallest fractional  
196 error in determination of the chemoattractant gradient direction due to the occupation  
197 state of receptors is:

198 
$$u_2 = v^{-1}T^{-3/2}(N_RSD)^{-1/2}c^{1/2}\varepsilon^{-1} \quad (2)$$

199 where  $v$  is the swimming velocity and  $\varepsilon = dc/dr$  is the chemoattractant concentration  
200 gradient (**Figure 1a**) (Berg and Purcell, 1977, Dusenbery, 2011, Vergassola et al.,  
201 2007). A locality requirement must also be met: the change in concentration across the  
202 distance spanned during  $T$  must be small, compared to the concentration itself

203 (Vergassola et al., 2007).

204 The slope of the chemoattractant concentration gradient  $\varepsilon$  directly impinges on the  
205 ability to reliably determine the source of the attractant (**Figure 1b**). At high  
206 concentrations of speract ( $10^{-8}$  to  $10^{-6}$  M) the change in receptor occupancy experienced  
207 by *S. purpuratus* spermatozoa, at two given distinct locations, allows the reliable  
208 assessment of the chemical gradient, when  $u_2 < 0.05$  (**Figure 1b**) (As for  $u_1$ ,  $u_2$  was  
209 considered to operate in the range  $[0, 1]$ ) (Vergassola et al., 2007, Berg and Purcell,  
210 1977). However, at low concentrations of speract (below of  $10^{-9}$  M), where other  
211 parameters are identical, stochastic fluctuations tend to dominate over the signal  
212 (**Figure 1b**). Under these low-concentration regimes, the slope of the chemoattractant  
213 gradient is determinant; shallow gradients ( $\varepsilon < 10^{-12}$  M  $\mu\text{m}^{-1}$ ) increase the uncertainty  
214 for detection of gradient polarity. In contrast, steeper chemoattractant gradients, *i.e.*  $\varepsilon \geq$   
215  $10^{-11}$  M  $\mu\text{m}^{-1}$ , would allow *S. purpuratus* spermatozoa to determine the orientation of  
216 the chemical gradient dependably (**Figure 1b**).

217 Previously it was shown that *L. pictus* spermatozoa experience chemotaxis in  
218 response to exposure to a gradient of speract (Guerrero et al., 2010a). Notably, under  
219 the same experimental regime *S. purpuratus* spermatozoa undergo a motility response  
220 to the presence of speract, yet do not demonstrate chemotaxis. It seems reasonable to  
221 speculate that the lack of chemotactic responses in *S. purpuratus* spermatozoa is due to  
222 their reduced receptor density relative to *L. pictus* spermatozoa. The chemoreception  
223 model predicts that, in contrast to *L. pictus*, *S. purpuratus* spermatozoa might determine  
224 the direction of the attractant gradient in the range of  $10^{-10}$  to  $10^{-9}$  M (**Figure 1b**, orange  
225 and yellow lines with  $u_2 < 5\%$ ), and thus can only determine the orientation of the  
226 chemical gradient in steep, but not shallow concentration gradients (**Figure 1b**, yellow  
227 and cyan lines with  $u_2 < 5\%$ ). If the latter holds to be true, then the model predicts that

228 *S. purpuratus* spermatozoa should be able to experience chemotaxis when exposed to  
229 relatively steep speract gradients, which have not been tested experimentally to date.

230 The ratio of uncertainties for reliable assessment of the direction of a speract gradient  
231 between *S. purpuratus* and *L. pictus* spermatozoa can be expressed as:

$$\frac{u_{2 \text{ purpuratus}}}{u_{2 \text{ pictus}}} = S \frac{\varepsilon_{\text{pictus}}}{\varepsilon_{\text{purpuratus}}},$$
$$S = \left( \frac{v_{\text{purpuratus}}}{v_{\text{pictus}}} \right)^{-1} \left( \frac{T_{\text{purpuratus}}}{T_{\text{pictus}}} \right)^{-3/2} \left( \frac{N_{R \text{ purpuratus}}}{N_{R \text{ pictus}}} \right)^{-1/2} \quad (3, 4)$$

234 with  $S$  being a factor that scales the slope of the speract gradient to a regime that  
235 allows *S. purpuratus* spermatozoa to detect the local direction of the chemical gradient.  
236 In other words, the model predicts that *S. purpuratus* spermatozoa should undergo  
237 chemotaxis in a speract gradient approximately three times steeper than the gradient that  
238 drives chemotaxis in *L. pictus* spermatozoa, with  $\varepsilon_{\text{purpuratus}} = 3.25 \varepsilon_{\text{pictus}}$ .

239 In summary, the chemoreception model suggests that *S. purpuratus* spermatozoa  
240 detect chemoattractant gradients with less sensitivity than those of *L. pictus*. It also  
241 predicts that *S. purpuratus* spermatozoa may detect chemoattractant gradients in the  $10^{-9}$   
242 M regime with sufficient certainty only if the difference in sampling concentration is  
243 greater than  $10^{-11}$  M  $\mu\text{m}^{-1}$  (steep concentration gradients) (**Figure 1b**). Given this  
244 prediction, we designed and implemented an experimental condition where *S.*  
245 *purpuratus* spermatozoa should experience chemotaxis.

246

### 247 ***S. purpuratus* spermatozoa accumulate at steep speract concentration gradients**

248 Our experimental setup is designed to generate specific concentration gradients by  
249 focusing a brief (200 ms) flash UV light along an optical fiber, through the objective,  
250 and into a field of swimming *S. purpuratus* spermatozoa containing CS at 10 nM in  
251 artificial sea water (Tatsu et al., 2002, Guerrero et al., 2010a). To test experimentally  
252 whether *S. purpuratus* undergo chemotaxis, as predicted from the chemoreception

253 model, we varied the slope of the chemoattractant gradient by separately employing  
254 four optical fibers of distinct diameters that could be arranged into five different  
255 configurations ( $f1$ ,  $f2$ ,  $f3$ ,  $f4$ ,  $f5$ ).

256 Each configuration produces a characteristic pattern of UV illumination within the  
257 imaging field (**Figure 2**). The UV intensity was measured at the back focal plane of the  
258 objective for each fiber configuration (**Figure 2a** and **Figure 2 – table supplement 1**).  
259 The spatial derivative of the imaged UV light profile was computed for use as a proxy  
260 for the slope of the speract concentration gradient (**Figure 2b**). By examining these UV  
261 irradiation patterns, we calculated that, at the gradient peak, the highest concentration of  
262 speract released through photo-liberation from CS is generated by the  $f5$  fiber, followed  
263 by  $f4 > f3 > f2 > f1$ . The steepest UV irradiation gradients are those generated by the  $f2$ ,  
264  $f3$  and  $f5$  fibers (**Figure 2b**).

265 Irrespective of the optical fiber used, the photo-activation of caged speract triggers  
266 the stereotypical  $Ca^{2+}$ -dependent motility responses of *S. purpuratus* spermatozoa  
267 (**Figure 2c**, **Movies 1, 2, 5, 6** and **7**). To determine whether these changes lead to sperm  
268 accumulation, we developed an algorithm which automatically scores the number of  
269 spermatozoa at any of four defined concentric regions (R1, R2, R3, and R4) relative to  
270 the center of the speract concentration gradient (**Figure 2 – figure supplement 1**).

271 Photo-liberation of speract through either  $f2$  or  $f3$  fiber, but not through  $f1$ ,  $f4$  or  $f5$   
272 fibers, lead to the accumulation of *S. purpuratus* spermatozoa towards the center of the  
273 speract gradient (zones R1 and R2) within the first 5-10 seconds after UV irradiation  
274 (**Figure 3**, **Figure 3 - figure supplement 1**, **Figure 3 - figure supplement 2**, **Movies 1**,  
275 **and 2**).

276 Interestingly, for  $f2$ , the number of spermatozoa increases in R1 and R2 and  
277 decreases in R3 and R4, indicating that cells from the R3 and R4 regions most probably

278 relocate towards R1 and R2 (**Figure 3a, Figure 3 - figure supplement 2 and Movie 1**). In  
279 the case of the  $f3$  gradient, the number of spermatozoa increases in the R1, R2 and R3  
280 regions and decreases in the R4 region, suggesting that spermatozoa in R4 and possibly  
281 outside of the imaged field are entering the other regions (**Figure 3a and Movie 2**). The  
282 maximum sperm accumulation (about two-fold) occurs in R1 for the  $f3$  gradient (**Figure**  
283 **3a and Movie 2**).

284 In the case of exposure to the  $f5$  speract concentration gradient the number of  
285 spermatozoa showed a tendency to increase in R2, R3 and R4, although it was only  
286 statistically significant in R4 (**Figure 3a, Figure 3 - figure supplement 2 and Movie**  
287 **6**). Gradients  $f1$ ,  $f4$  and negative controls (Low  $[Ca^{2+}]_i$  or High  $[K^+]_e$ ) did not show  
288 increased sperm number in any region (**Figure 3a, Figure 3 - figure supplement 1,**  
289 **Figure 3 - figure supplement 2, Movies 3, 4, 5 and 6**).

290 We also evaluated the corresponding  $[Ca^{2+}]_i$  changes across the imaging field for  
291 each imposed speract concentration gradient. Gradients  $f2$  to  $f5$  increase  $[Ca^{2+}]_i$  in  
292 spermatozoa at least two-fold, while the increase for the  $f1$  gradient was modest (**Figure**  
293 **3b**). Interestingly,  $[Ca^{2+}]_i$  levels rose highest upon exposure to the  $f4$  gradient, even  
294 though the number of spermatozoa did not increase significantly (**Figure 3a**), which  
295 underlines the notion that elevated  $[Ca^{2+}]_i$  levels are necessary, but not sufficient to  
296 drive the accumulation of spermatozoa (**Figure 3**), as previously suggested (Kaupp et  
297 al., 2003, Wood et al., 2005, Bohmer et al., 2005, Guerrero et al., 2010a, Alvarez et al.,  
298 2012).

299 In summary, *S. purpuratus* spermatozoa accumulate towards the center of the speract  
300 gradients generated by the  $f2$ - and  $f3$ -fibers, which are the two optical fibers that  
301 generate UV light profiles with steeper slopes compared to the  $f1$  and  $f4$  fibers (**Figure**  
302 **2b**). Notably, use of fibers  $f4$  and  $f5$  photo-releases higher concentrations of speract (by

303 providing higher UV energies than other fibers) (**Figure 2a, Figure 2 table**  
304 **supplement 1**), yet they trigger neither the maximum accumulation of *S. purpuratus*  
305 spermatozoa at the center of the chemoattractant field, nor the most elevated  $[Ca^{2+}]_i$   
306 response.

307

308 *S. purpuratus* spermatozoa undergo chemotaxis upon exposure to steep speract  
309 gradients

310 The spatial derivative of the UV profiles shown in **Figure 2b** indicates that the  
311 steeper light gradients generated from UV irradiation are those of *f2*, *f3* and *f5*, which  
312 are assumed to generate the most pronounced speract gradients of similar form. This  
313 assumption is strictly only valid at the instant of UV exposure, as subsequently the  
314 speract gradient dissipates over time with a diffusion constant of  $D \approx 240 \mu m^2 s^{-1}$ .

315 We further sought to understand how the stimulus function, which *S. purpuratus*  
316 spermatozoa experience during the accumulation of bound speract throughout their  
317 trajectory, influences their motility response. For this purpose, we computed the spatio-  
318 temporal dynamics of the speract gradient for *f1*, *f2*, *f3*, *f4* and *f5* fibers (**Figure 4a, b**  
319 and **Figure 4 - figure supplement 1**) and analyzed the trajectories of spermatozoa  
320 swimming in these five distinct speract gradient configurations (**Figure 4c and Figure 4**  
321 **- figure supplement 2**). From these trajectories, we derived the chemotaxis indices  
322 (LECI, (Yoshida et al., 2002)) (**Figure 4d and Figure 5**), and computed the stimulus  
323 function of individual spermatozoa in response to each of the five speract gradient  
324 forms (**Figure 4e and Figure 4 - figure supplement 2**).

325 Fibers *f2*, *f3* and *f5* triggered chemotaxis in *S. purpuratus* spermatozoa (**Figure 4,**  
326 **Figure 4 - figure supplement 2 and Figure 5**). Under such conditions, only those  
327 spermatozoa located in the regions R3 and R4 at the moment of speract uncaging

328 underwent chemotaxis (**Figure 5**; see **Figure 4** and **Figure 4 - supplement figure 2** for  
329 single sperm reorienting towards the center of speract gradients generated by the  $f_2$  and  
330  $f_3$  fibers, respectively). For both,  $f_2$  and  $f_3$  conditions, sperm chemotaxis initiated within  
331 the first 3 s after speract exposure, and lasted less than 10 s (**Figure 5**, **Figure 3 - figure**  
332 **supplement 1**, **Movies 1** and **2**).

333 **Figure 4b** shows that, for the  $f_2$  condition, the slope of the speract gradient within  
334 R2 and regions is barely altered during the initial 3 seconds of speract exposure (gray  
335 shading). Spermatozoa in that region sample a pseudo-static speract gradient over a  
336 short (2-3 s) period, which is apparently sufficient to permit detection of the direction of  
337 the gradient. In contrast, spermatozoa located at other regions (R1, R3, R4) experience a  
338 speract gradient with a slope that changes during the sampling time (**Figure 4a, 4b**).

339 In summary,  $f_2$ ,  $f_3$  and  $f_5$  optical fibers generate speract concentration gradients that  
340 drive the accumulation of *S. purpuratus* spermatozoa. Of note, the  $f_4$  fiber generates a  
341 speract gradient that activates motility responses of *S. purpuratus* spermatozoa but not  
342 chemotaxis (**Movie 6**), although it was previously shown that it triggers the  
343 accumulation of *L. pictus* spermatozoa (Guerrero et al., 2010a).

344 The model of chemoreception presented in the previous section (**equations (3, 4)**)  
345 predicts a scaling rule for chemotactic responses between *S. purpuratus* and *L. pictus*  
346 spermatozoa of  $S > 3.25$ . Moreover, the UV-irradiation profiles shown in **figure 2b**  
347 indicate that  $f_2$ ,  $f_3$ , and  $f_5$  fibers generate steeper speract gradients than  $f_4$  fiber.

348 To reliably determine the direction of the chemoattractant concentration gradient, the  
349 signal difference  $dc$  between two sampled positions  $dr$  must be greater than the noise  
350 (**Figure 1a**). In order to test the prediction of the chemoreception model, we computed  
351 the local relative slope  $\xi$  detected by single spermatozoa exposed to a given speract  
352 concentration gradient, with  $\xi = c^{-1/2} dc/dr$  (**Figure 4e**).

353 We found that, in agreement with the chemoreception model, the maximum relative  
354 slope  $\xi_{max} = \text{Max}(\xi_1, \xi_2, \xi_3, \dots, \xi_n)$  experienced by *S. purpuratus* spermatozoa, when  
355 exposed to  $f_2$  and  $f_3$  speract gradients, were up to 2-3 times greater than that  
356 experienced when exposed to the  $f_4$ -generated speract gradient (**Figure 6a**). In addition,  
357 they were also up to 2-3 times greater than the relative slope experienced by *L. pictus*  
358 spermatozoa when exposed to  $f_4$  speract gradient (**Figure 6a**), hence supporting the  
359 predicted scaling rule for the detection of the speract concentration gradient between *L.*  
360 *pictus* and *S. purpuratus* spermatozoa.

361

362 **The slope of the speract gradient is the critical determinant for the strength of**  
363 **coupling between the stimulus function and the internal  $\text{Ca}^{2+}$  oscillator**

364 To test the idea that the slope of the speract gradient regulates the coupling between  
365 the stimulus function and the internal  $\text{Ca}^{2+}$  oscillator triggered by speract, we made use  
366 of a generic model for coupled phase oscillators (Pikovsky et al., 2001). In its simplest  
367 form, the model describes two phase oscillators of intrinsic frequencies  $\omega_1$  and  $\omega_2$   
368 coupled with a strength  $\gamma$  through the antisymmetric function of their phase difference  $\phi$   
369  $= \varphi_1 - \varphi_2$ . The time evolution of  $\phi$  then follows an Adler equation  $d\phi/dt = \Delta\omega - 2\gamma \sin(\phi)$ ,  
370 which is the leading order description for weakly-coupled non-linear oscillators. In the  
371 present case, the two coupled oscillators are the internal  $\text{Ca}^{2+}$  oscillator and the  
372 oscillations in the stimulus function induced in spermatozoa swimming across a speract  
373 gradient. The former occurs even for immotile cells, for which there are no stimulus  
374 oscillations under a spatially uniform speract field (**Figure 6 - supplement 1**, and  
375 **Movie 8**); while the latter exists under two tested negative controls: cells swimming in  
376 Low  $\text{Ca}^{2+}$  and in High  $\text{K}^+$  artificial sea water, both of which inhibit  $\text{Ca}^{2+}$  oscillations (see  
377 **Figure 3, Movie 3 and 4**).

378 There are two immediate predictions from the Adler model: first, there is a minimum  
379 coupling strength necessary for the two oscillators to synchronize ( $\gamma_{min} = \Delta\omega/2$ ). For  
380 weaker coupling (*i.e.*  $\gamma < \gamma_{min}$ ), the two oscillators run with independent frequencies and,  
381 hence, the phase difference increases monotonically with time; second, and within the  
382 synchronous region (*i.e.*  $\gamma > \gamma_{min}$ ), the phase difference between the oscillators is  
383 constant and it does not take any arbitrary value, but rather follows a simple relation to  
384 the coupling strength ( $\phi_{sync} = \arcsin(\Delta\omega/2\gamma)$ ). **Figure 6b** shows the two regions in the  
385 parameter space given by  $\Delta\omega$  and  $\gamma$ . The boundary between these two regions  
386 corresponds to the condition  $\gamma = \gamma_{min}$  and it delimits what is known as an Arnold's  
387 tongue.

388 We measure the difference in intrinsic frequency by looking at the instantaneous  
389 frequency of the internal  $\text{Ca}^{2+}$  oscillator just before and after the speract gradient is  
390 established. The range of measured  $\Delta\omega$  is shown in the same figure as a band of  
391 accessible conditions in our experiments (mean of  $\Delta\omega$ , black line; mean  $\pm$  standard  
392 deviation, green dashed lines). If the driving coupling force between the oscillators is  
393 the maximum slope of the speract gradient, *i.e.*  $\gamma = \xi_{max}$ , we would expect to find a  
394 minimum slope ( $\overline{\xi_{max}^*}$ ) below which no synchrony is observed.

395 This is indeed the case as clearly shown in **Figure 6a**, **6c** and **6d** (magenta line).  
396 Moreover, and for cells for which synchronization occurs, the measured phase  
397 difference is constrained by the predicted functional form of  $\phi_{sync} = \phi_{sync}(\Delta\omega, \gamma)$  as can  
398 be verified from the collapsed data shown in **Figure 6c**, and **6d** within the theoretical  
399 estimates.

400 Altogether, the excellent agreement of this simple model of coupled phase oscillators  
401 with our data, points to the slope of the speract gradient as the driving force behind the  
402 observed synchronous oscillations and, as a result, for the chemotactic ability of sea

403 urchin spermatozoa.

## 404 Discussion

405 Marine spermatozoa, together with many motile microorganisms, explore their  
406 environment via helical swimming paths, whereupon encountering a surface these  
407 helices collapse to circular trajectories. The intrinsic periodicity of either swimming  
408 behavior commonly results in the periodic sampling of the cells chemical environment  
409 with direct implications for their ability to accurately perform chemotaxis.

410 A strict requirement for sperm chemotaxis is the presence of extracellular  $\text{Ca}^{2+}$ . For  
411 chemotaxis to occur, the timing of the  $\text{Ca}^{2+}$  transients (*i.e.* the intracellular  $\text{Ca}^{2+}$   
412 oscillations) triggered by the chemoattractants must also be kept in phase with the  
413 polarity of the chemoattractant concentration field, which in this, and other studies, is  
414 referred as the stimulus function (Bohmer et al., 2005, Guerrero et al., 2010a, Kaupp et  
415 al., 2008, Friedrich and Jülicher, 2008). This requisite coupling ensures that the turning  
416 events start at the descending phase of the chemoattractant concentration field;  
417 otherwise spermatozoa are driven away by  $\text{Ca}^{2+}$ -dependent motility adjustments. The  
418 periodic sampling of chemoattractants by the sperm flagellum continuously feeds back  
419 to the signaling pathway governing the intracellular  $\text{Ca}^{2+}$  oscillator, hence providing a  
420 potential coupling mechanism for sperm chemotaxis. Indirect evidence for the existence  
421 of a feedback loop operating between the stimulus function and the  $\text{Ca}^{2+}$  oscillator  
422 triggered by chemoattractants has been found in *L. pictus*, *A. punctulata* and *Ciona*  
423 *intestinalis* species, whose spermatozoa show robust chemotactic responses towards  
424 their conspecific chemoattractants (Guerrero et al., 2010a, Shiba et al., 2008, Jikeli et  
425 al., 2015, Bohmer et al., 2005).

426 For almost three decades, chemotaxis had not been observed for the widely studied  
427 *S. purpuratus* species under diverse experimental conditions, raising doubts about their  
428 capabilities to ‘sense’ and respond to the spatial cues provided by the speract

429 concentration gradients. To tackle whether *S. purpuratus* spermatozoa are able to  
430 ‘sense’ a chemoattractant concentration gradient, we use a model of chemoreception  
431 developed by Berg and Purcell, which considers the minimal requirements needed for a  
432 single searcher (*i.e.* a sperm cell) to gather sufficient information to determine the  
433 orientation of a non-uniform concentration field. By considering the difference between  
434 *L. pictus* and *S. purpuratus* spermatozoa in terms of the number of chemoattractant  
435 receptors, receptor pocket size, sampling time, swimming velocity, sampling distance,  
436 and the local mean and slope of the chemoattractant concentration field, we predicted  
437 that *S. purpuratus* should be able to detect the polarity of a speract concentration field.  
438 The model predicts that speract gradient necessary to guide *S. purpuratus* spermatozoa  
439 would be up to three times steeper than the gradient that drives chemotactic responses  
440 on *L. pictus* spermatozoa. We tested this prediction experimentally by exposing *S.*  
441 *purpuratus* spermatozoa to various defined speract concentration gradients. We show  
442 that *S. purpuratus* spermatozoa exhibit chemotactic responses but, as predicted by the  
443 chemoreception model, only if the speract concentration gradients are sufficiently steep  
444 (*i.e.* speract gradients that are at least three times steeper than the speract concentration  
445 gradient that drives chemotaxis in *L. pictus* spermatozoa). The shallower speract  
446 gradients previously tested are therefore unable to generate any chemotactic response in  
447 *S. purpuratus* spermatozoa.

448 To investigate further the molecular mechanism involved in sperm chemotaxis, we  
449 measured both the stimulus function and the triggered-internal  $\text{Ca}^{2+}$  oscillations for up  
450 to five hundred *S. purpuratus* spermatozoa exposed to five distinct speract  
451 concentration gradients. We demonstrate that the slope of the chemoattractant  
452 concentration field is a major determinant for sperm chemotaxis in *S. purpuratus*, and  
453 might be an uncovered feature of sperm chemotaxis in general. A steep slope of the

454 speract gradient entrains the frequencies of the stimulus function and the internal  $\text{Ca}^{2+}$   
455 oscillator triggered by the periodic sampling of a non-uniform speract concentration  
456 field. We assessed the transition boundary of the coupling term (the slope of the speract  
457 concentration field) for the two oscillators to synchronize, and found it to be very close  
458 to the boundary where *S. purpuratus* start to experience chemotaxis. The agreement of  
459 our data with a model of weakly coupled phase oscillators, points to the slope of the  
460 speract gradient as the driving force behind the observed synchronous oscillations and,  
461 as a result, for the chemotactic ability of sea urchin spermatozoa.

462 One can further hypothesize about the evolutionary origin of the described  
463 differences in sensitivity to chemoattractant concentration gradients between *S.*  
464 *purpuratus* and *L. pictus* spermatozoa given the significant differences between their  
465 ecological reproduction niches. The turbulent environment where sea urchin reproduce  
466 directly impinges on the dispersion rates of small molecules such as speract, hence,  
467 imposing ecological pressure against sperm chemotaxis. For instance, the reproduction  
468 success of *L. pictus*, *S. purpuratus* and *Abalone* species has been shown to peak at  
469 particular hydrodynamic shearing values (Zimmer and Riffell, 2011, Riffell and  
470 Zimmer, 2007, Mead and Denny, 1995, Hussain et al., 2017). We might ask what are  
471 the typical values of the chemoattractant gradients encountered by the different species  
472 in their natural habitats. The correct scale to consider when discussing the small-scale  
473 distribution of chemicals in the ocean is the Batchelor scale,  $l_B = (\eta D^2 / \zeta)^{1/4}$ , where  $\eta$  is  
474 kinematic viscosity,  $D$  the molecular diffusivity and  $\zeta$  is the turbulent dissipation rate  
475 (Batchelor, 2006, Aref et al., 2014). Turbulence stirs dissolved chemicals in the ocean,  
476 stretching and folding them into sheets and filaments at length scales down to the  
477 Batchelor scale: below  $l_B$  molecular diffusion dominates and chemical gradients are  
478 smoothed out.

479 *S. purpuratus* is primarily found in the low intertidal zone. The purple sea urchin  
480 thrives amid strong wave action and areas with churning aerated water. These more  
481 energetic zones, including tidal channels and breaking waves, generate relatively high  
482 levels of turbulence ( $\zeta \sim 10^{-4} \text{ m}^2\text{s}^{-3}$ ) which lead to relatively small values of  $l_B$  and,  
483 hence, to steep gradients (*i.e.*  $1/l_B$ ). *L. pictus*, on the contrary, is mostly found at the edge  
484 of or inside kelp beds, well below the low tide mark where the levels of turbulence are  
485 much more moderate ( $\zeta \sim 10^{-6} \text{ m}^2\text{s}^{-3}$ ) (Jiménez, 1997, Thorpe, 2007). This difference in  
486 turbulent kinetic energy dissipation rate has a significant effect on the largest chemical  
487 gradients available in a particular habitat for sperm chemotaxis. The ratio of  $l_B$  for the  
488 different habitats scales as  $l_{B\text{purpuratus}}/l_{B\text{pictus}} \sim (\zeta_{\text{pictus}}/\zeta_{\text{purpuratus}})^{1/4} \sim 3$ , which fits  
489 considerably well with the relative sensitivity to speract of the two species.  
490 Furthermore, we have shown that *S. purpuratus* spermatozoa experience chemotaxis  
491 toward steeper speract gradients than those that guide *L. pictus* spermatozoa, which is  
492 also compatible with the distinct chemoattractant gradients they might naturally  
493 encounter during their voyage searching for the egg.

494 The chemoattractant concentration gradients generated in the present study were  
495 near-instantaneously set up by the photo-release of speract in still water. Further  
496 experimental studies are needed to assess the chemotactic ability of sea urchin  
497 spermatozoa to more realistic chemoattractant gradients (as those shaped, for instance,  
498 by hydrodynamic forces in their natural environment) and to shed light into the  
499 mechanisms governing chemotaxis and their ecological implications.

500

## 501 **Materials and Methods**

### 502 *Materials*

503 Undiluted *S. purpuratus* or *L. pictus* spermatozoa (Pamanes S. A. de C. V.,  
504 Ensenada, Mexico and Marinus Scientific, LLC. Newport Beach, CA, USA  
505 respectively) were obtained by intracoelomic injection of 0.5 M KCl and stored on ice  
506 until used within a day. Artificial seawater (ASW) was 950 to 1050 mOsm and  
507 contained (in mM): 486 NaCl, 10 KCl, 10 CaCl<sub>2</sub>, 26 MgCl<sub>2</sub>, 30 MgSO<sub>4</sub>, 2.5 NaHCO<sub>3</sub>,  
508 10 HEPES and 1 EDTA (pH 7.8). For experiments with *L. pictus* spermatozoa, slightly  
509 acidified ASW (pH 7.4) was used to reduce the number of spermatozoa experiencing  
510 spontaneous acrosome reaction. Low Ca<sup>2+</sup> ASW was ASW but pH 7.0 and with 1 mM  
511 CaCl<sub>2</sub>, and Ca<sup>2+</sup>-free ASW was ASW with no added CaCl<sub>2</sub>. [Ser5; nitrobenzyl-  
512 Gly6]speract, referred to throughout the text as caged speract (CS), was prepared as  
513 previously described (Tatsu et al., 2002). Fluo-4-AM and pluronic F-127 were from  
514 Molecular Probes, Inc. (Eugene, OR, USA). PolyHEME [poly(2-  
515 hydroxyethylmethacrylate)] was from Sigma-Aldrich (Toluca, Edo de Mexico,  
516 Mexico).

### 517 *Loading of Ca<sup>2+</sup>-fluorescent indicator into spermatozoa*

518 Undiluted spermatozoa were suspended in 10 volumes of low Ca<sup>2+</sup> ASW containing  
519 0.2% pluronic F-127 plus 20 μM of fluo-4-AM and incubated for 2.5 h at 14 °C.  
520 Spermatozoa were stored in the dark and on ice until use.

### 521 *Imaging of fluorescent swimming spermatozoa*

522 The cover slips were briefly immersed into a 0.1% wt/vol solution of poly-HEME in  
523 ethanol, hot-air blow-dried to rapidly evaporate the solvent and mounted on reusable  
524 chambers fitting a TC-202 Bipolar temperature controller (Medical Systems Corp.). The  
525 temperature plate was mounted on a microscope stage (Eclipse TE-300; Nikon) and

526 maintained at a constant 15 °C. Aliquots of labeled sperm were diluted in ASW and  
527 transferred to an imaging chamber (final concentration  $\sim 2 \times 10^5$  cells  $\text{ml}^{-1}$ ).  
528 Epifluorescence images were collected with a Nikon Plan Fluor 40x 1.3 NA oil-  
529 immersion objective using the chroma filter set (ex HQ470/40x; DC, 505DCXRU; em,  
530 HQ510LP) and recorded on a DV887 iXon EMCCD Andor camera (Andor Bioimaging,  
531 NC). Stroboscopic fluorescence illumination was supplied by a Cyan LED no. LXHL-  
532 LE5C (Lumileds Lighting LLC, San Jose, USA) synchronized to the exposure output  
533 signal of the iXon camera (2 ms illumination per individual exposure). Images were  
534 collected with AndoriQ 1.8 software (Andor Bioimaging, NC) at 30.80 fps in full-chip  
535 mode (observation field of 200 x 200  $\mu\text{m}$ ).

#### 536 *Image processing*

537 The background fluorescence was removed by generating an average pixel intensity  
538 time-projection image from the first 94 frames before uncaging, which was then  
539 subtracted from each frame of the image stack by using the Image calculator tool of  
540 ImageJ 1.49u (Schneider et al., 2012). For **Figure 2c**, the maximum pixel intensity time  
541 projections were created every 3 s from background-subtracted images before and after  
542 the UV flash.

#### 543 *Quantitation of global changes of spermatozoa number and $[\text{Ca}^{2+}]_i$*

544 To study the dynamics of overall sperm motility and  $[\text{Ca}^{2+}]_i$  signals trigger by the  
545 distinct speract gradients, we developed an algorithm that provides an efficient  
546 approach to automatically detect the head of every spermatozoa in every frame of a  
547 given video-microscopy (C/C++, OpenCV 2.4, Qt-creator 2.4.2). Fluorescence  
548 microscopy images generated as described previously were used. The following steps  
549 summarize the work-flow of the algorithm (**Figure 2 - figure supplement 1**):

550 1. Segment regions of interest from background: This step consists of thresholding

551 each image (frame) of the video (x, y, t) to segment the zones of interest (remove  
552 noise and atypical values). Our strategy includes performing an automatic  
553 selection of threshold value for each Gaussian blurred image ( $I_G$ ) ( $\sigma = 3.5 \mu\text{m}$ )  
554 considering the mean value ( $M_I$ ) and the standard deviation ( $S_I$ ) of the image  $I_G$ .  
555 The threshold value is defined by:  $T_I = M_I + 6S_I$ .

556 2. Compute the connected components: The connected components labeling is used  
557 to detect connected regions in the image (a digital continuous path exists between  
558 all pairs of points in the same component - the sperm heads). This heuristic  
559 consists of visiting each pixel of the image and creating exterior boundaries using  
560 pixel neighbors, accordingly to a specific type of connectivity.

561 3. Measure sperm head fluorescence. For each region of interest, identify the  
562 centroid in the fluorescence channel (sperm head) and measure the mean value.

563 4. Compute the relative positions of the sperm heads within the imaging field, and  
564 assign them to either R1, R2, R3 or R4 concentric regions around the centroid of  
565 the UV flash intensity distribution. The radii of R1, R2, R3 or R4, were 25, 50,  
566 75 and 100  $\mu\text{m}$ , respectively.

567 5. Repeat steps 1 to 4 in a frame-wise basis.

568 Step 1 of the algorithm filters out shot noise and atypical values; step 2 divides the  
569 images in N connected components on the location of the sperm heads; step 3  
570 quantitates sperm head fluorescence, and finally step 4 computes the relative sperm  
571 position on the imaging field. A similar approach has been recently used to identify  
572 replication centers of adenoviruses in fluorescence microscopy images (Garces et al.,  
573 2016).

574 We automatically analyzed up to 267 videos of *S. purpuratus* spermatozoa, each  
575 containing tens of swimming cells, exposed to five distinct speract concentration

576 gradients.

577 *Computing the dynamics of speract concentration gradients*

578 The dynamics of the chemoattractant gradient was computed using the Green's  
579 function of the diffusion equation:

$$580 \quad c(r, t) = \frac{c_0}{\sqrt{2\pi}\sigma} e^{-r^2/2\sigma^2} + C_b \quad (5)$$

581 This equation for the concentration tells us that the profile has the form of a  
582 Gaussian. The width of the Gaussian is  $\sigma = \sqrt{4D(t + t_0)}$ , and hence it increases as the  
583 square root of the time.  $C_b$  is the basal concentration of the chemoattractant,  $D$  is the  
584 molecular diffusivity.

585 The speract concentration gradients were generated via the photolysis of 10 nM  
586 caged speract (CS) with a 200 ms UV pulse delivered through each of four different  
587 optical fibers with internal diameters of 200  $\mu\text{m}$ , 600  $\mu\text{m}$ , 2 mm and 4 mm (at two  
588 different positions). Light intensity was normalized dividing each point by the sum of  
589 all points of light intensity for each fiber and multiplying it by the fiber potency  
590 (measured at the back focal plane of the objective) in milliwatts (mW) (**Figure 2 - table**  
591 **supplement 1**). Each spatial distribution of instantaneously-generated speract  
592 concentration gradient was computed by fitting their corresponding normalized spatial  
593 distribution of UV light (Residual standard error:  $2.738 \times 10^{-5}$  on 97 degrees of  
594 freedom), considering an uncaging efficiency of 5%, as reported (Tatsu et al., 2002).

595 The diffusion coefficient of a molecule is related to its size by the Stokes-Einstein  
596 equation:

$$597 \quad D = \frac{kT}{6\pi\eta R_h} \quad (6)$$

598 where  $k$  is Boltzmann's constant,  $T$  is the temperature,  $\eta$  is the viscosity of the  
599 solvent, and  $R_h$  is the hydrodynamic radius (Lakowicz, 2006). The hydrodynamic radius

600  $R_h$  of speract was calculated by modeling the molecules in terms of equivalent  
601 hydrodynamic spheres.

$$602 \quad R_h = \left( \frac{3M\bar{v}}{4\pi} \right)^{1/3} \quad (7)$$

603 where  $M$  is the molecular weight, and  $\bar{v}$  is the specific gravity (Lakowicz, 2006). The  
604 volume of an equivalent spherical particle is  $V_e = 4/3 \pi R_h^3$ . Equations 6 and 7 show  
605 that the radius and diffusion coefficient are weakly dependent on the molecular weight.

606 The diffusion coefficient of speract has not been measured experimental, nonetheless  
607 it can be estimated following equations 6 and 7. The diffusion coefficient of a similar  
608 chemoattractant molecule, resact (with fourteen amino acids), has been reported,  $D_{resact}$   
609  $= 239 \pm 7 \mu\text{m}^2 \text{s}^{-1}$  (Kashikar et al., 2012). If we consider that speract is a decapeptide,  
610 the 1.4 fold difference in molecular weight between speract and resact would imply a  
611  $(1.4)^{1/3}$  fold difference in their diffusion coefficients, which is close to the experimental  
612 error reported (Kashikar et al., 2012). For the sake of simplicity, the spatio-temporal  
613 dynamics of the distinct instantaneously generated speract gradients was modeled  
614 considering a speract diffusion coefficient of  $D_{speract} = 240 \mu\text{m}^2 \text{s}^{-1}$ .

615 The hydrodynamic radius of speract ( $R_h = 8.8 \text{ \AA}$ ) was computed with equation (6),  
616 with  $D_{speract} = 240 \mu\text{m}^2 \text{s}^{-1}$ ,  $k = 1.38 \times 10^{-23} \text{ J K}^{-1}$ ,  $T = 288.15 \text{ K}$  and  $\eta = 0.001 \text{ N s /m}^2$ .

617 *Computing  $[Ca^{2+}]_i$  dynamics, chemotactic behavior, and the stimulus function of*  
618 *single spermatozoa*

619 Spermatozoa were tracked semi-automatically by following the head centroid with the  
620 MtrackJ plugin (Meijering et al., 2012) of ImageJ 1.49u. Single cell  $[Ca^{2+}]_i$  signals were  
621 computed from the mean value of a 5 x 5 pixels region, centered at each sperm head  
622 along the time.

623 Chemotactic behavior was quantified using the linear equation chemotaxis index  
624 (*LECI*) employing different temporal windows before (control) and after uncaging

625 speract. *LECI* is defined as the negative value of the slope ( $LECI = -l$ ) of a least square  
626 linear regression  $r(t) = lt + r_0$  (Yoshida et al., 2002) where  $r(t)$  is the sperm head  
627 distance to the center of the speract concentration gradient,  $t$  is the time after UV pulse  
628 measured in seconds, with  $t \in [0 - 3; 3.2 - 6.2; 6.2 - 9.2]$  seconds. Positive *LECI* indicate  
629 movement towards the chemoattractant source. The center of the speract gradient was  
630 identified as the centroid of the UV flash intensity distribution.

631 The head position of each spermatozoa was used to compute the local concentration  
632 of speract at  $r(x, y)$  over each frame. The stimulus function of single spermatozoa  
633  $s = c(r, t)$  was computed by solving equation (5), considering both their swimming  
634 trajectories, and the spatio-temporal evolution of a given speract concentration gradient.  
635 The profiles of UV light were used to compute the initial conditions at  $c(r, t_0)$ .

636 The phase- and temporal-shifts between time derivative of the stimulus function  
637  $ds/dt$  and the internal  $Ca^{2+}$  oscillator triggered by speract, were computed from their  
638 normalized cross-correlation function.

639 *Analysis of speract induced  $Ca^{2+}$  transients with immobilized spermatozoa.*

640 Imaging chambers were prepared by coating cover slips with 50  $\mu\text{g/ml}$  poly-D-  
641 lysine, shaking off excess, and allowing to air-dry. Coated cover slips were then  
642 attached to imaging chambers. Fluo-4 labeled spermatozoa were diluted 1:40 in ASW,  
643 immediately placed into the chambers, and left for 2 min, after which unattached sperm  
644 were removed by washing with ASW. The chambers were then filled with 0.5 ml of  
645 ASW containing 500 nM of caged speract, and mounted in a TC-202 Bipolar  
646 temperature controller (Medical Systems Corp.). Images were collected with Andor iQ  
647 1.7 software (Andor Bioimaging, NC) at 90 fps in full-chip mode, binning 4x4  
648 (observation field of 200  $\mu\text{m}$  x 200  $\mu\text{m}$ ). The imaging setup was the same as that used  
649 for swimming spermatozoa. The caged speract was photo-released with a 200 ms UV

650 pulse delivered through an optical fiber (4 mm internal diameter) coupled to a Xenon  
651 UV lamp (UVICO, Rapp Opto Electronic). The optical fiber was mounted on a  
652 “defocused” configuration to minimized the generation of UV light heterogeneities.

653 Images were processed off-line using ImageJ 1.4.5s. Overlapping spermatozoa and  
654 any incompletely adhered cells, which moved during the experiment, were ignored.  
655 Fluorescence measurements in individual sperm were made by manually drawing a  
656 region of interest around the flagella with the line tool of ImageJ.

657 Programs were written in R statistical software.

658

## 659 **Theory**

660 *Constraints over the detection of chemoattractant concentration fields.*

661 Strategies for chemoattractant sampling based on local concentration gradients require  
662 the concentration to be high enough to ensure that the measured average difference at  
663 two nearby locations is larger than typical fluctuations (Wood et al., 2015). As  
664 stochastic fluctuations limits the precision with which a microorganism can, in a given  
665 time  $T$ , determine the concentration of a surrounding chemoattractant (Berg and Purcell,  
666 1977, Vergassola et al., 2007), the rate of encounter between a chemoattractant  $c$   
667 diffusing with effective diffusivity  $D$  and its receptor, with a binding site of effective  
668 radius  $s$ , is given by:

$$669 \quad J(\mathbf{r}) = 4\pi s D c(\mathbf{r}) \quad (8)$$

670 For reliable assessment of the local concentration  $c(r)$ , a spermatozoon provided with  
671  $N_R$  number of chemoattractant receptors, collects detection events over time  $T_{int}$ . The  
672 average number of detection events will then be  $J(r)N_RT_{int}$ . Typical stochastic  
673 fluctuations are of the order of the square root of the mean (Berg and Purcell, 1977).  
674 Then the condition for the signal to emerge from the noise reads:

$$675 \quad \sqrt{N_R S D c T_{int}} \ll 1 \quad (9)$$

676 Then, it follows that the spermatozoon will experience an uncertainty  $u_1 =$   
 677  $(N_R S D c T_{int})^{-1/2}$  (eq. (1)), for measuring a variation on the local concentration of  
 678 chemoattractant (**Figure 1 - figure supplement 1**).

679

680 To reliably measure a concentration gradient of chemoattractant, the difference in  
 681 counts collected by the spermatozoon in the interval measurement must be above the  
 682 noise level (**Figure 1a**). The corresponding conditions can be stated as (Berg and  
 683 Purcell, 1977, Vergassola et al., 2007):

$$684 \quad \left( v T_{int} \frac{dc}{dr} \right) N_R S D T_{int} \gg \sqrt{N_R S D c T_{int}} \quad (10)$$

$$685 \quad v T_{int} \frac{d \log c}{dr} \ll 1 \quad (11)$$

686 Here,  $v$  is the swimming velocity and  $dc/dr$  is the concentration gradient of the  
 687 chemoattractant. The first inequality indicates that the signal-to-noise ratio for the  
 688 difference in the number of hits experienced by the swimming spermatozoon across the  
 689 integration time  $T_{int}$  be larger than unity. The second inequality is the requirement of  
 690 locality, *i.e.* the change in concentration across the distance spanned during  $T_{int}$  needs  
 691 to be small compared to the local concentration itself.

692 The information to determine the direction of the chemoattractant gradient results  
 693 from the magnitude difference of the signal at two sampled positions. Then the  
 694 condition for the signal to emerge from the noise on a chemoattractant field reads:

$$695 \quad v^{-1} T^{-3/2} (N_R S D)^{-1/2} c^{1/2} \varepsilon^{-1} \ll 1 \quad (12)$$

696 where  $\varepsilon = dc/dr$  is the chemoattractant concentration gradient. Then, it follows that  
 697 the least fractional error of the chemoattractant gradient direction due to the state of  
 698 occupation of receptors is  $u_2 = v^{-1} T^{-3/2} (N_R S D)^{-1/2} c^{1/2} \varepsilon^{-1}$  (**Figure 1, eq. (2)**).

699 Assuming an exponentially decaying concentration, reliable integration time  $T_{int}$   
700 scales as  $exp(r/3\lambda)$  (Vergassola et al., 2007).

#### 701 *Statistical analyses*

702 Data are presented for individual spermatozoa (n) collected from up to three sea  
703 urchins. All statistical tests were performed using R software (R Core Team, 2016). The  
704 significance level was set at 95%.

705

#### 706 **Acknowledgements**

707 The authors thank Dr. Tatsu Yoshiro for providing the caged speract, and Drs.  
708 Hermes Gadêlha, David Smith and Nina Pastor for stimulating discussions and a critical  
709 reading of the manuscript. AG thanks Dr. Manabu Yoshida and Dr. Kaoru Yoshida for  
710 feedback about sperm chemotaxis in marine invertebrates, and to the Japan Society for  
711 the Promotion of Science (JSPS invitation fellowship for research in Japan to A.G.,  
712 short term JSPS/236, ID no. S16172).

713

#### 714 **Author contributions**

715 A.G., A.D. and I.T. conceived the project; A.G. and V.J.S. performed the  
716 experiments; H.R.G., A.G., I.T., V.J.S. and M.V. analyzed the data; A.G., I.T. and  
717 H.R.G performed the mathematical model calculations and wrote the corresponding  
718 section; A.D., A.G., H.R.G. and I.T. participated in the design and drafting of the  
719 manuscript J.C., C.D.W. and C.B. provide feedback for conceptualization and drafting  
720 of the manuscript. All authors approved the final version of the article.

721

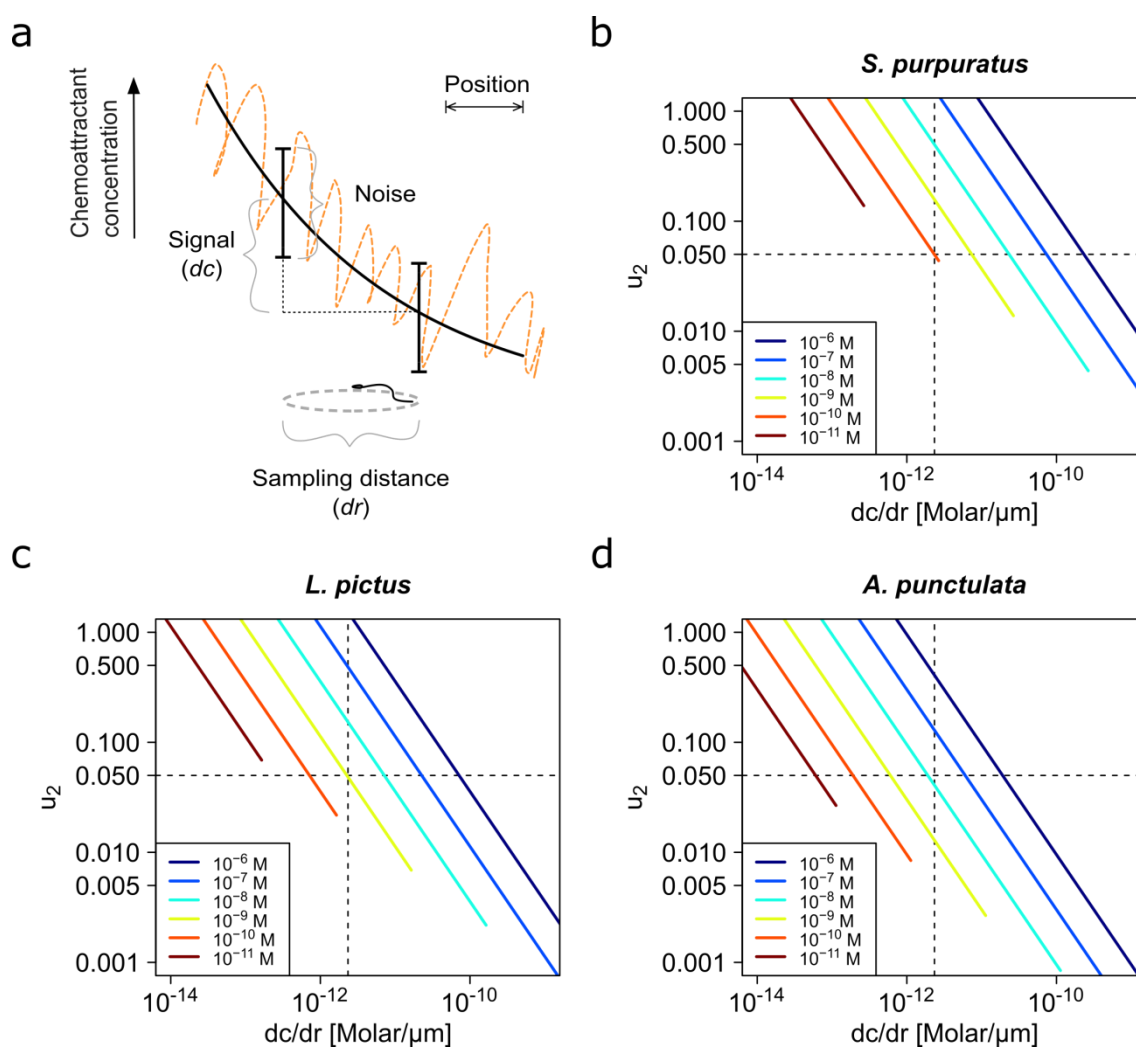
#### 722 **Competing interests**

723 The authors declared that no competing interests exist.

724

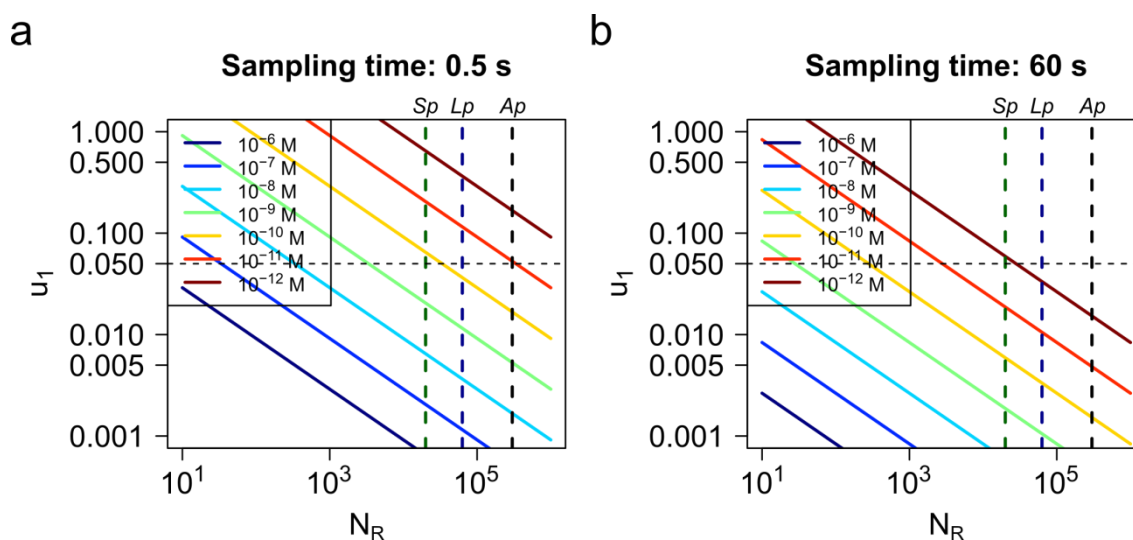
725 **Funding**

726 A.D. and A.G. acknowledges grants from the Consejo Nacional de Ciencia y  
727 Tecnología (CONACyT Fronteras 71, CONACyT Ciencia Básica 252213), A.G., A.D.  
728 and C.B to Programa de Apoyo a Proyectos de Investigación e Innovación Tecnológica  
729 UNAM (PAPIIT/DGAPA) (IA202417, IN205516, IN206016 and IN112514  
730 respectively). We acknowledge CONACYT and PAPIIT for fellowships to M.V.P.; the  
731 Spanish Ministry of Economy and Competitiveness Grants No. FIS2013-48444-C2-1-P,  
732 FIS2016-77692-C2-1- P, the Subprogram Ramón-y-Cajal and the Ibero-America  
733 Program-Santander Universities 2015 (I.T.).



734

735 **Figure 1. Physics of chemoreception.** **a.** Determining the direction of the  
 736 chemoattractant gradient requires that the signal difference  $dc$  between two sampled  
 737 positions  $dr$  must be greater than the noise. **b-d.** The uncertainty in the determination of  
 738 the chemoattractant gradient direction,  $u_2$ , plotted against the slope of the gradient,  
 739  $dc/dr$ , in log-log scale, for different chemoattractant concentrations, **(b)** *S. purpuratus*,  
 740 **(c)** *L. pictus*, and **(d)** *A. punctulata* spermatozoa (See **Figure 1 - table supplement 1** for  
 741 the list of parameter values taken in consideration for panels **b-d**).



742

743 **Figure 1 - figure supplement 1. Uncertainty for the detection of a homogeneous**  
 744 **chemoattractant concentration field.** The uncertainty for determining the  
 745 chemoattractant concentration  $u_I$  versus the receptor number  $N_R$  for different  
 746 concentrations ( $10^{-6}$  to  $10^{-12}$  M), for a sampling interval of  $T = 0.5$  s **(a)**, or a  $T = 60$  s  
 747 **(b)**. Vertical lines indicate the number of receptors of Sp = *S. purpuratus* (dark green),  
 748 Lp = *L. pictus* (dark blue) and Ap = *A. punctulata* (black) spermatozoa. Parameters:  
 749 sampling interval  $T = 0.5$  s **(a)** and 60 s **(b)**, speract diffusion coefficient  $D = 239 \mu\text{m}^2\text{s}^{-1}$ ,  
 750  $^1$ , hydrodynamic radius of speract (as proxy of receptor pocket size)  $R_h = 0.79$  nm (see  
 751 **figure 1 - figure supplement 2 and figure 1 - table supplement 1).**

<i>Spermatozoan species</i>	<i>S. purpuratus</i>	<i>L. pictus</i>	<i>A. punctulata</i>
$N_R$ [per cell]	$2 \times 10^{4b}$	$6.3 \times 10^{4b}$	$3 \times 10^5$
$D$ [ $\text{cm}^2\text{s}^{-1}$ ]	$2.4 \times 10^{-6c}$	$2.4 \times 10^{-6c}$	$2.4 \times 10^{-6c}$
$s$ [cm]	$1.65 \times 10^{-7c}$	$1.65 \times 10^{-7c}$	$1.65 \times 10^{-7c}$
$T$ [s]	$0.39 \pm 0.08^a$	$0.52 \pm 0.22^a$	0.6
$v$ [ $\text{cm}\text{s}^{-1}$ ]	$121 \pm 13 \times 10^{-4a}$	$144 \pm 36 \times 10^{-4a}$	$200 \times 10^{-4}$
$dr$ [cm]	$28 \pm 6 \times 10^{-4a}$	$46 \pm 14 \times 10^{-4a}$	$60 \times 10^{-4}$

752

753 **Figure 1 - table supplement 1. Parameters of the chemoattractant sampling model**

754 **for each species.** Note that the main differences between species are the number of

755 receptors  $N_R$  and the velocity  $v$  of the spermatozoon.  $D$  diffusion coefficient;  $s$

756 hydrodynamic radius of speract (as proxy of chemoattractant receptor's pocket radius);

757  $T$  sampling time (time to swim half circumference in the boundary close to the water-

758 glass interface);  $dr$  = sampling interval (circumference diameter). <sup>a</sup>Measured in this

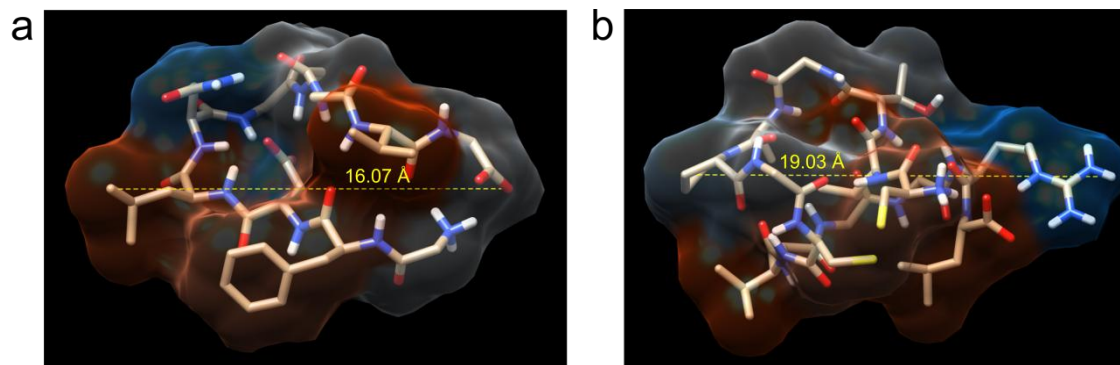
759 study (mean  $\pm$  sd;  $N = 3$  sea urchins;  $n = 495$  (*S. purpuratus*), 56 (*L. pictus*)

760 spermatozoa. <sup>b</sup>(Nishigaki et al., 2001, Nishigaki and Darszon, 2000). <sup>c</sup>Calculated in this

761 study (see section: *Computing the dynamics of speract concentration gradients* in

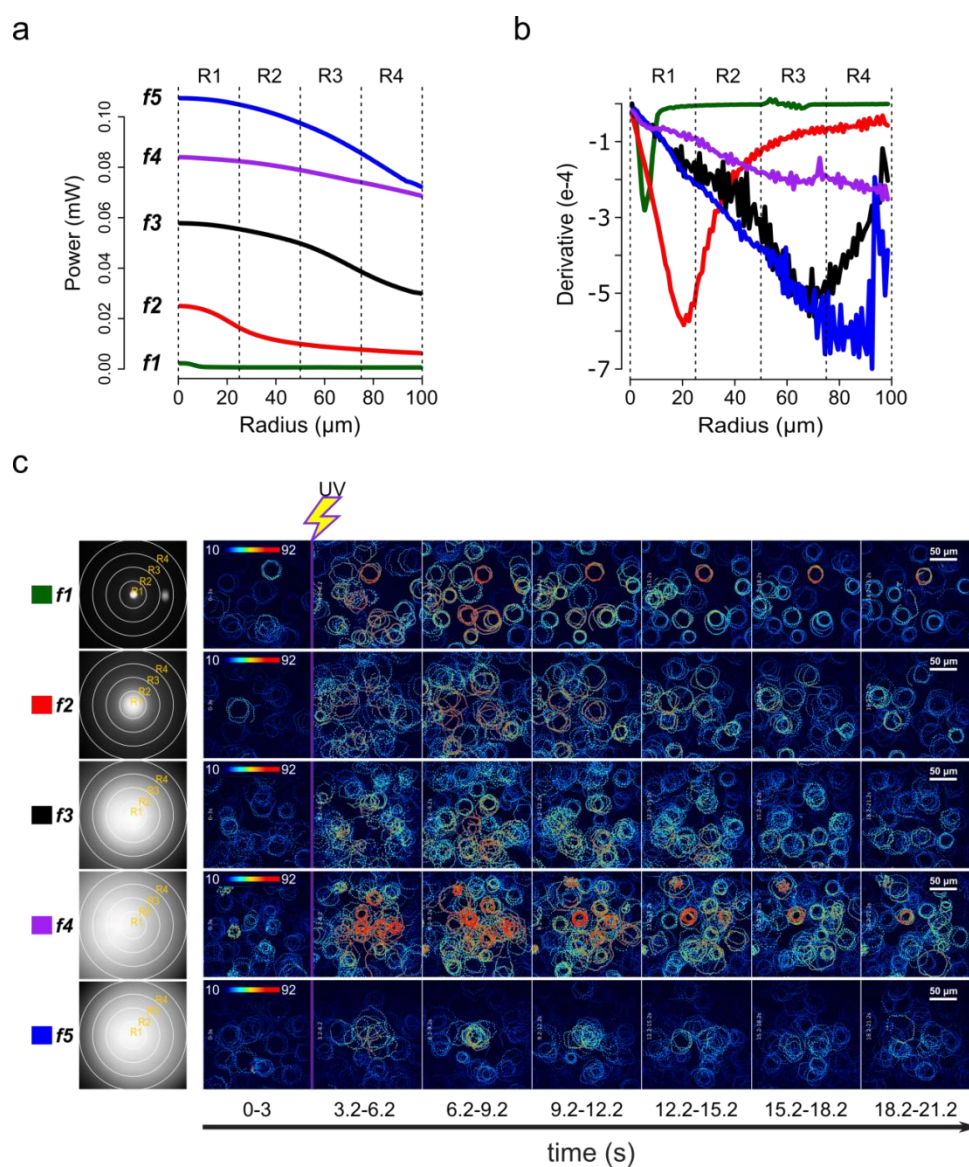
762 **Materials and Methods, and Figure 1 - figure supplement 2).**

763



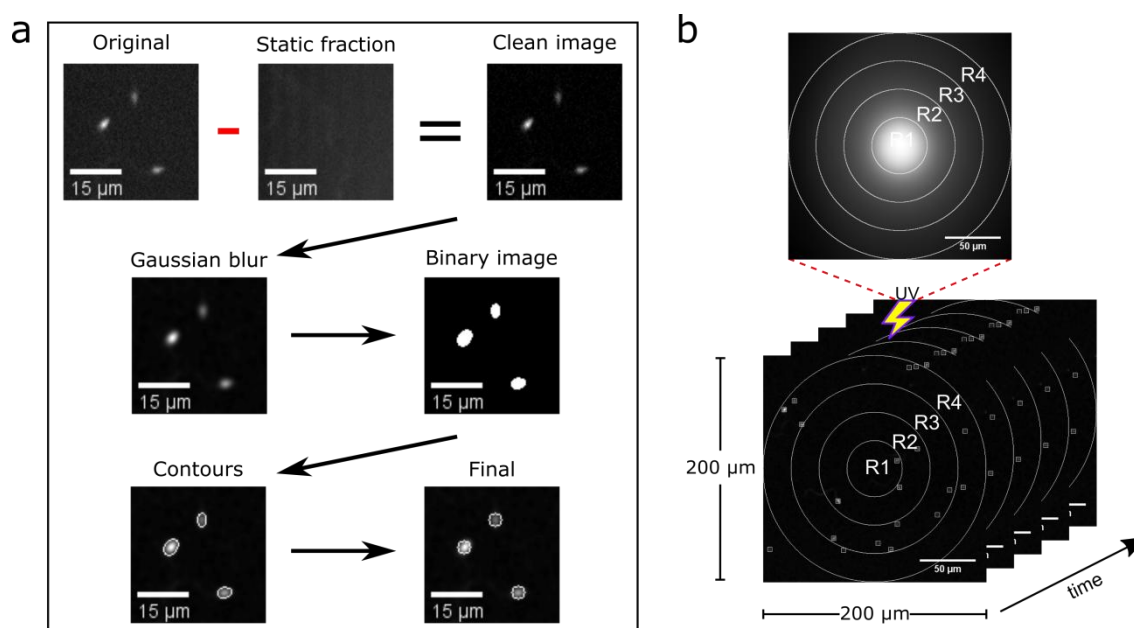
764

765 **Figure 1 - figure supplement 2. Speract and resact modeling.** Five speract and resact  
766 structures, respectively, were modeled using PEP-FOLD (Maupetit et al., 2009,  
767 Thevenet et al., 2012, Maupetit et al., 2010), and used to estimate an equivalent  
768 hydrodynamic radius by computing the length of the mayor axis of each model: **a.**  
769 Speract ( $16.18 \pm 0.41 \text{ \AA}$ ). **b.** Resact ( $18.97 \pm 1.79 \text{ \AA}$ ). The estimates of the mayor axis  
770 of the speract model were similar to their corresponding hydrodynamic diameter  
771 estimates ( $d = 2R_h = 2(8) \text{ \AA} = 1.6 \text{ nm}$ ) computed with the Stokes-Einstein equation ( $R_h$   
772  $= 0.88 \text{ nm}$ ) (see section: *Computing the dynamics of speract concentration gradients* in  
773 **Materials and Methods**). Models were visualized with chimera 1.11.2 (Pettersen et al.,  
774 2004).



775

776 **Figure 2. Screening of speract concentration gradients.** **a.** Radial profile of the UV  
 777 light scattered at the glass-liquid interface for each optical fiber (*f1-f5*). **b.** Derivatives of  
 778 radial distribution for each optical fiber. **c.** Spatial distribution of the UV flash energy  
 779 (left), and typical motility and  $[\text{Ca}^{2+}]_i$  responses of spermatozoa exposed to different  
 780 concentration gradients of speract (right). F-F<sub>0</sub> time projections, showing spermatozoa  
 781 head fluorescence each 3 s before and after 200 ms UV photoactivation of 10 nM caged  
 782 speract in artificial sea water. The pseudo-color scale represents the relative  
 783 fluorescence of fluo-4, a  $\text{Ca}^{2+}$  indicator, showing maximum (red) and minimum (blue)  
 784 relative  $[\text{Ca}^{2+}]_i$ . Scale bars of 50  $\mu\text{m}$ .



786 **Figure 2 - figure supplement 1. Automatic segmentation of swimming**  
787 **spermatozoa. a.** Working-flow of the algorithm: Video microscopy images were  
788 background subtracted by removing the temporal average intensity projection (static  
789 fraction) of the first un-stimulated frames (93 frames = 3 seconds) from the whole video  
790 (25 seconds). The resulting images were convolved with a low-pass spatial frequency  
791 filter to eliminate typical detector shot-noise. The resulting images were thresholded to  
792 generate arrays of regions of interest (ROIs), a heuristic search for connected  
793 components is then applied to label single ROIs and to assign the corresponding pixels  
794 to unique spermatozoa. Scale bar of 15  $\mu\text{m}$ . **b.** The positions of the sperm heads within  
795 the imaging field are assigned to either R1, R2, R3 or R4 concentric regions around the  
796 centroid of the UV flash intensity distribution. Each ROI was also used to compute the  
797 sperm head fluorescence from the raw video microscopy images (as the mean value of  
798 the ROI). Scale bar of 50  $\mu\text{m}$ .

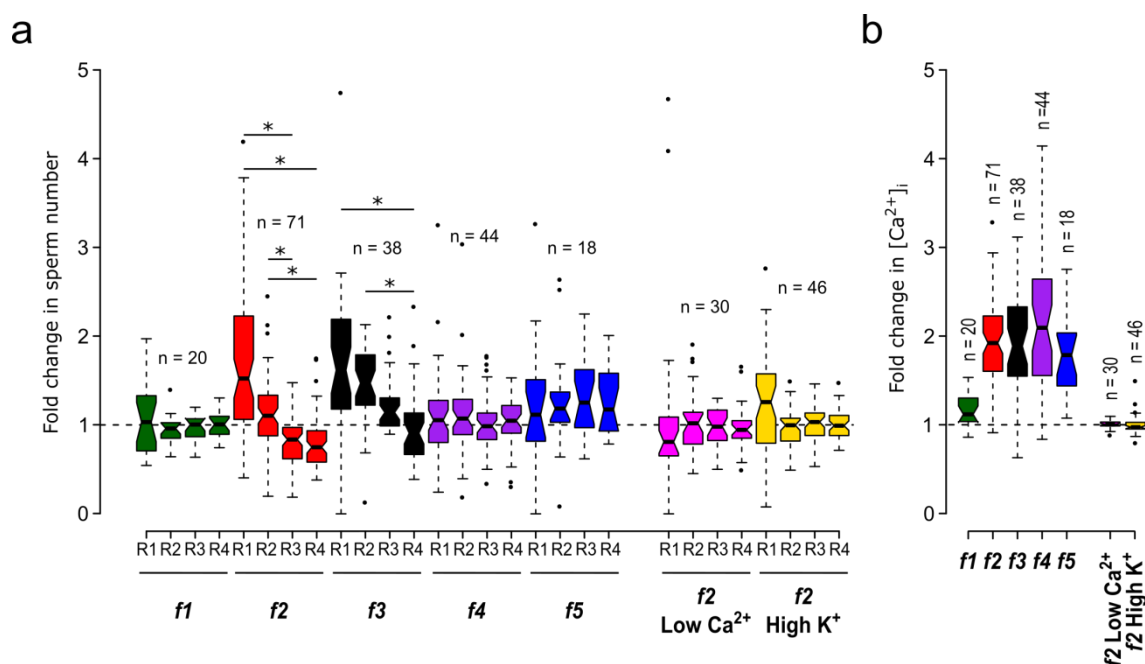
799

	Physical diameter (mm)	UV power at the back focal plane of the objective (mW)*
<i>f1</i>	0.2	0.07
<i>f2</i>	0.6	1.25
<i>f3</i>	2	4.7
<i>f4</i>	4	7.8
<i>f5</i>	4	9.46

800

801 **Figure 2 - table supplement 1. Physical diameter of the optical fibers, and UV light**  
802 **power measured at the back focal plane of a 40×/1.3NA oil-immersion objective.**

803 \*Typically, there is a 20% loss of light power due to scattering within the optics.



804

805 **Figure 3. Motility and [Ca<sup>2+</sup>]<sub>i</sub> responses of *S. purpuratus* spermatozoa exposed to**

806 **specific concentration gradients of speract. a.** Fold change in sperm number, defined

807 as the number of spermatozoa at the peak of the response (6 s) relative to the mean

808 number before speract stimulation (0-3 s) (see **figure 3 - figure supplement 1**). **b.**

809 Relative changes in [Ca<sup>2+</sup>]<sub>i</sub> experienced by spermatozoa at the peak response (6 s) after

810 speract stimulation. Negative controls for spermatozoa chemotaxis are artificial sea

811 water with nominal Ca<sup>2+</sup> (Low Ca<sup>2+</sup>); and artificial sea water with 40 mM of K<sup>+</sup> (High

812 K<sup>+</sup>). Both experimental conditions prevent chemotactic responses by inhibiting the Ca<sup>2+</sup>

813 membrane permeability alterations triggered by speract; the former disrupts the Ca<sup>2+</sup>

814 electrochemical gradient, and the later disrupt the K<sup>+</sup> electrochemical gradient required

815 as electromotive force needed for the opening of Ca<sup>2+</sup> channels. Number of experiments

816 (n) on the top of each experimental condition. Each box contains 50% of single events,

817 the inner lines indicate the median and the error bars delimit the 95% outliers. The

818 notch display a confidence interval around the median (median +/- 1.57 x IQRn<sup>-1/2</sup>). If

819 two boxes notches do not overlap, there is evidence that their medians differ (95%

820 confidence). \*Statistical significance, p < 0.05; Multiple comparison test after Kruskal-

821 Wallis. Studies at the population level are presented in **figure 3 - figure supplement 1**,  
822 while studies considering the absolute number of spermatozoa at two periods: 3s and 6s  
823 (3 seconds before and after speract exposure, respectively) are presented in **figure 3 -**  
824 **figure supplement 2**.  
825

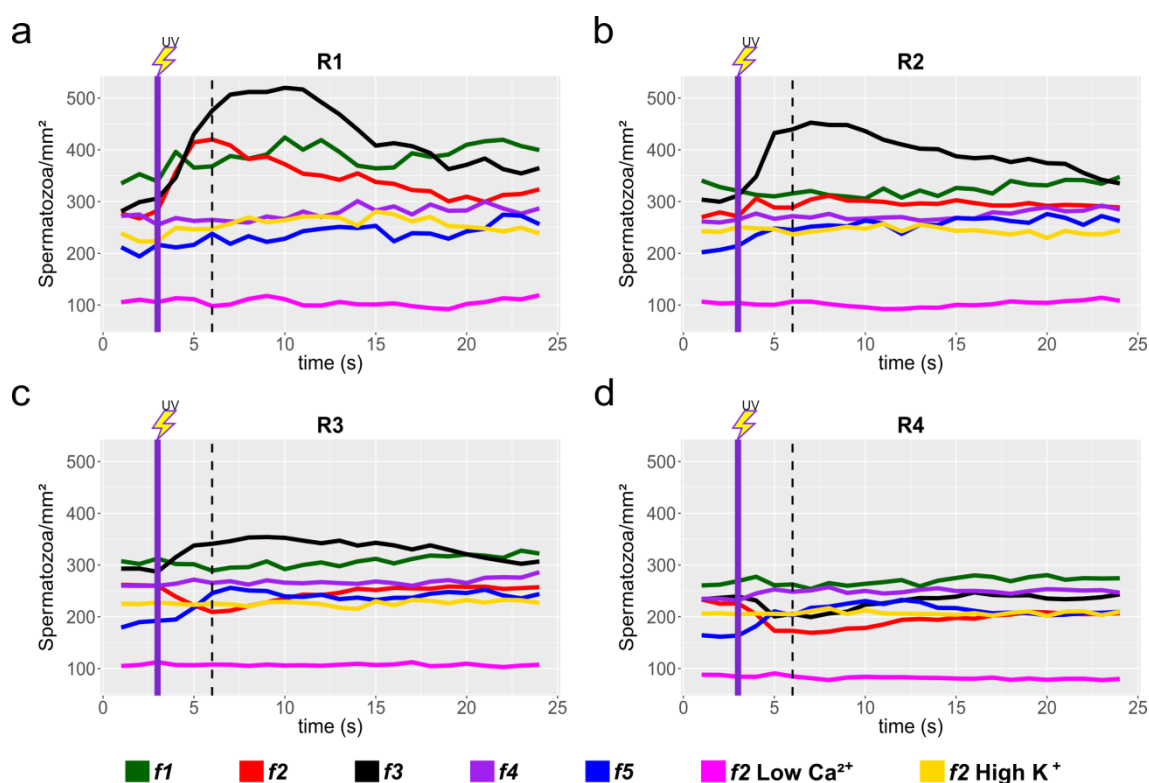
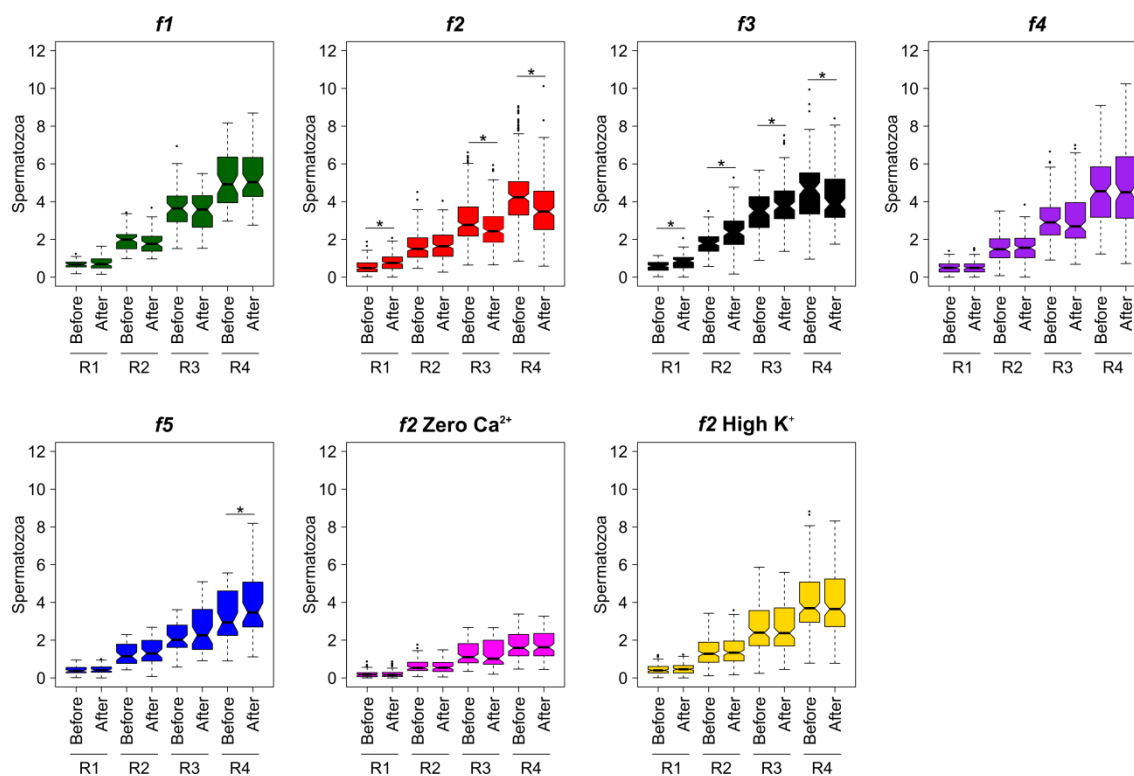
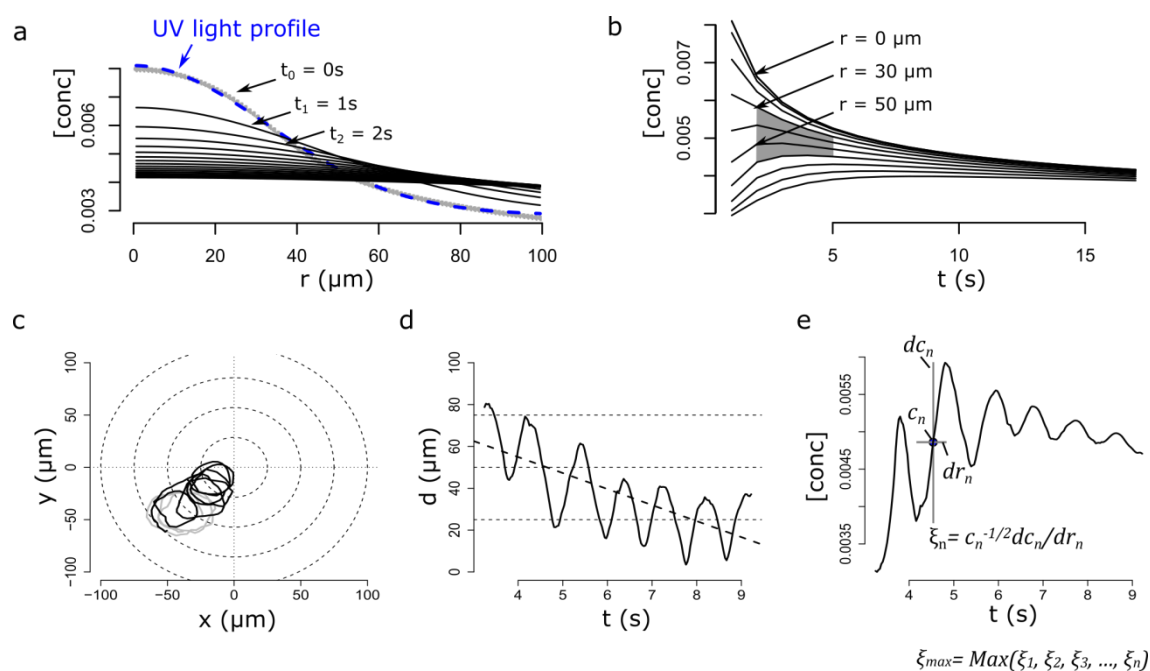


**Figure 3 - figure supplement 1. Sperm response to speract photo-release, collated data from individual experiments.** Sperm motility responses to different speract concentration gradients (*f1*, *f2*, *f3*, *f4*, *f5*) at R1 (a), R2 (b), R3 (c) and R4 (d) concentric regions. Negative controls for sperm chemotaxis are artificial sea water with nominal 0  $\text{Ca}^{2+}$  (Low  $\text{Ca}^{2+}$ ); and artificial sea water with 40 mM of  $\text{K}^+$  (High  $\text{K}^+$ ). Each time trace, represent the mean sperm density from up to 20 video microscopy experiments (raw data distributions at two periods 3s and 6s are presented in **figure 3 - figure supplement 2**). Note that peak responses occurred at second 6, three seconds after speract exposure (indicated as vertical dotted lines).



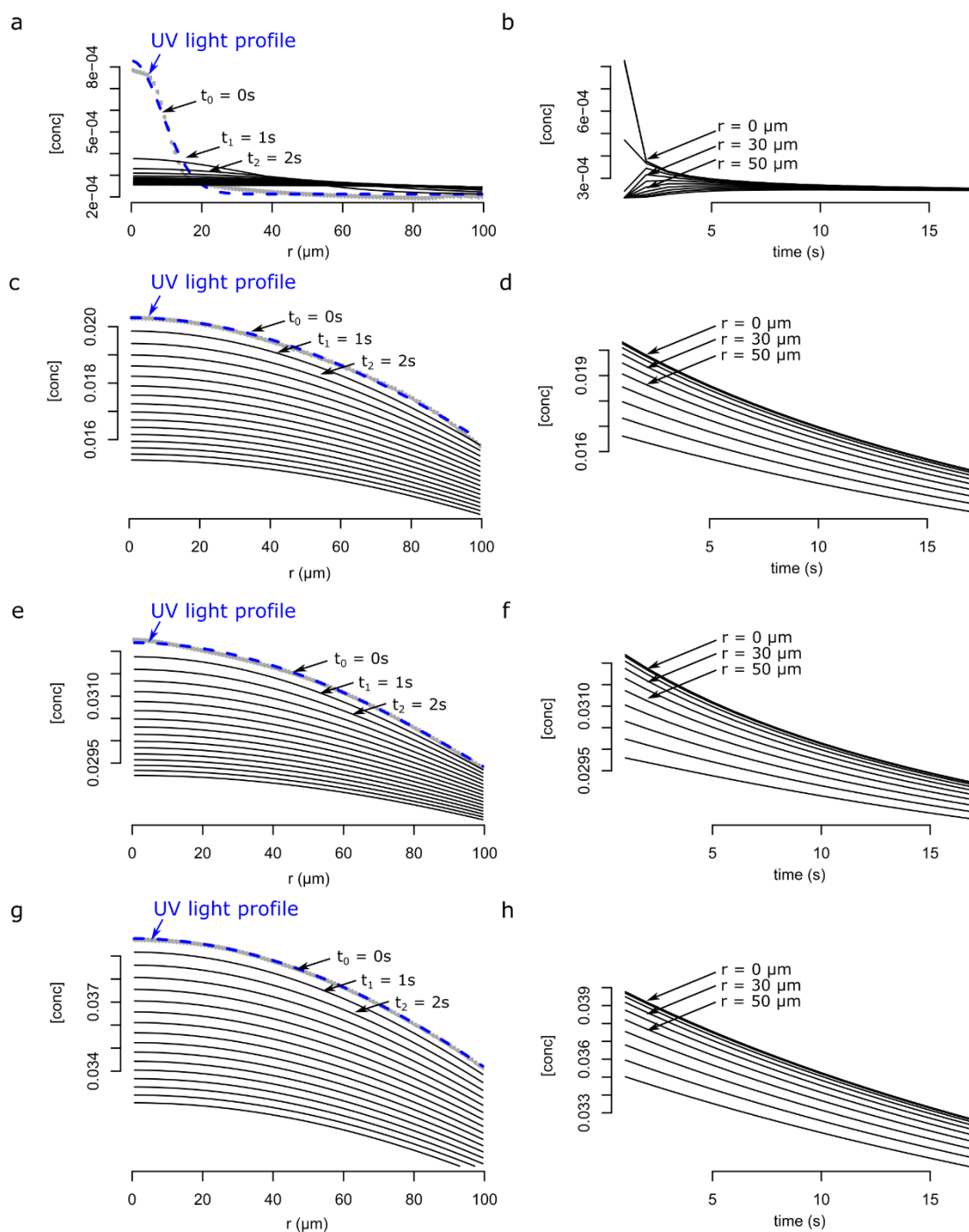
837

838 **Figure 3 - figure supplement 2. Absolute number of sperm cells, three seconds**  
839 **before and three seconds after speract photo-release through either *f1, f2, f3, f4, f5***  
840 **optical fibers. Absolute number of spermatozoa scored at either R1, R2, R3 or R4**  
841 **concentric regions around the centroid of the UV flash intensity distribution. Each box**  
842 **contains 50% of single events, the inner lines indicate the median and the error bars**  
843 **delimit the 95% outliers. \*Statistical significance,  $p < 0.05$ ; Mann-Whitney test.**



844

845 **Figure 4. Steep speract gradients attract *S. purpuratus* spermatozoa.** **a.** Dynamics  
 846 of the *f2* speract gradient. The blue dashed line ( $t_0 = 0$  s) corresponds to a Gaussian  
 847 distribution fitted to the UV light profile, and illustrates the putative shape of the  
 848 instantaneously-generated speract concentration gradient. Solid black lines illustrate the  
 849 temporal evolution of the speract concentration field after  $t = 1, 2, 3, \dots, 20$  seconds. **b.**  
 850 Temporal changes in *f2* speract field computed radially (each 10  $\mu\text{m}$ ) from the center of  
 851 the gradient. A region where the concentration of speract barely changes is shown in  
 852 gray. **c.** Characteristic motility changes of a *S. purpuratus* spermatozoon exposed to the  
 853 *f2* speract gradient. Solid lines illustrate its swimming trajectory 3 s before (gray) and 6  
 854 s after (black) speract exposure. **d.** Spermatozoon head distance to the source of the  
 855 speract gradient versus time, calculated from black trajectory in c. LECI index is  
 856 computed from the least squared linear regression of the head distance to the source, a  
 857 negative slope (as shown) indicates chemotaxis (positive LECI). **e.** Stimulus function  
 858 computed from the swimming behavior of the spermatozoon in c, considering the  
 859 dynamics of a.



860

861 **Figure 4 - figure supplement 1. Modeling of the dynamics of speract gradient**

862 **based on the UV light profile of distinct optical fibers.** The radial profiles of the UV

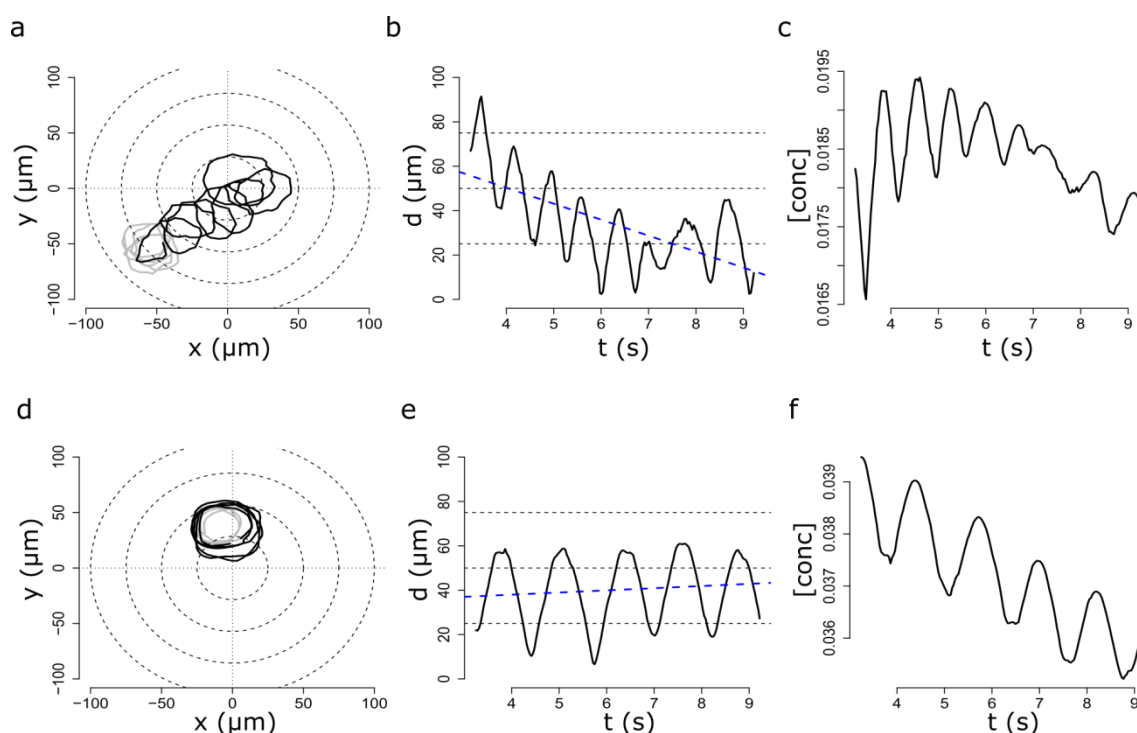
863 light scattered at the glass-liquid interface of *f1*, *f3*, *f4*, *f5* optical fibers are shown in

864 gray. The speract gradient was generated as in **figure 4**, but with the corresponding *f1*

865 **(a)**, *f3* **(c)**, *f4* **(e)** and *f5* **(g)** optical fibers. *Left panels* - The dynamics of the speract

866 gradient computed as is in **figure 4**. The blue dashed line ( $t_0 = 0$ ) corresponds to a

867 Gaussian distribution fitted to the UV light profile, and illustrates the putative shape of  
868 the instantaneously generated speract gradient. Solid black lines illustrate the shape of  
869 the speract gradient after  $t = 1, 2, 3, \dots, 20$  seconds. *Right panels* - Simulated temporal  
870 changes in speract concentration gradients of  $f1$  (**a**),  $f3$  (**c**),  $f4$  (**e**) and  $f5$  (**g**) at each 10  
871 radial  $\mu\text{m}$  point from the center of the concentration gradient.



872

873 **Figure 4 - figure supplement 2. Characteristic motility changes of a *S. purpuratus***

874 **spermatozoon exposed to *f3* and *f4* speract gradients (chemotactic vs non-**

875 **chemotactic response). Panels a, b and c show single cell responses to the *f3* speract**

876 **gradient (chemotactic); and panels d, e and f to the *f4* speract gradient (non-**

877 **chemotactic). a, d. Solid lines illustrate the spermatozoon swimming trajectory 3 s**

878 **before (gray) and 6 s after (black) speract gradient exposure. b, e. Spermatozoon head**

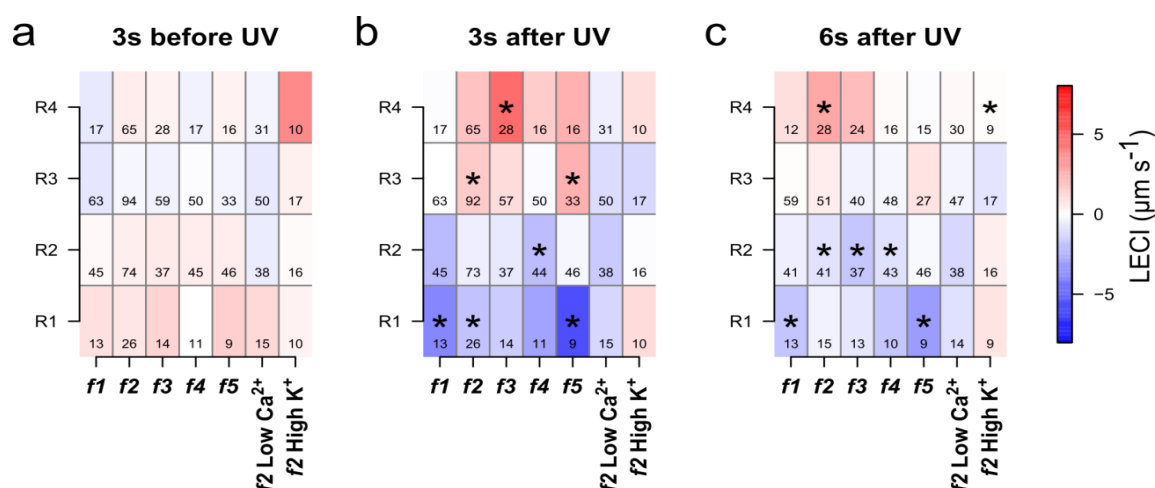
879 **distance to the source of the speract gradient versus time calculated from a and d,**

880 **respectively. b, e. Stimulus function computed from a and d, considering the spatio-**

881 **temporal dynamics of speract computed for the *f3* and *f4* gradients, respectively.**

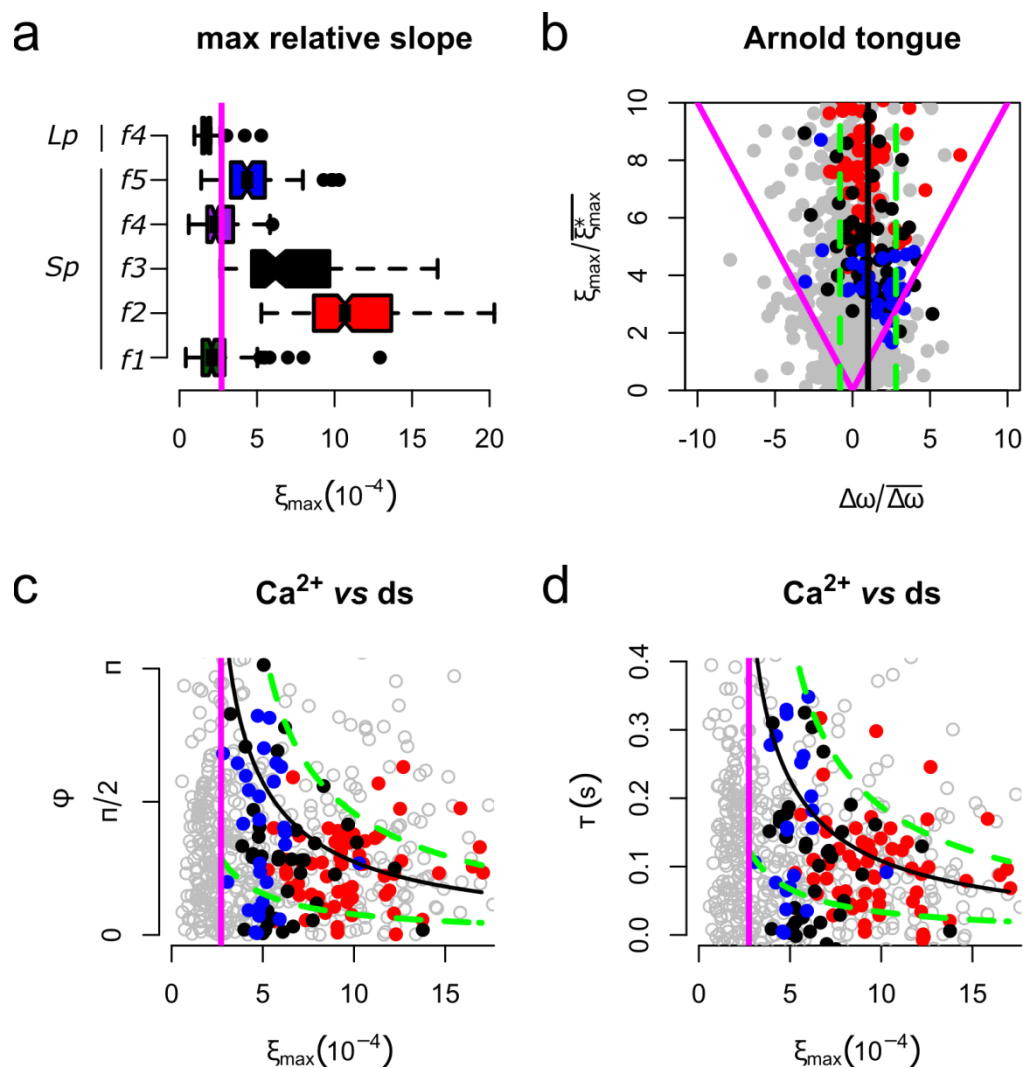
882

883



884

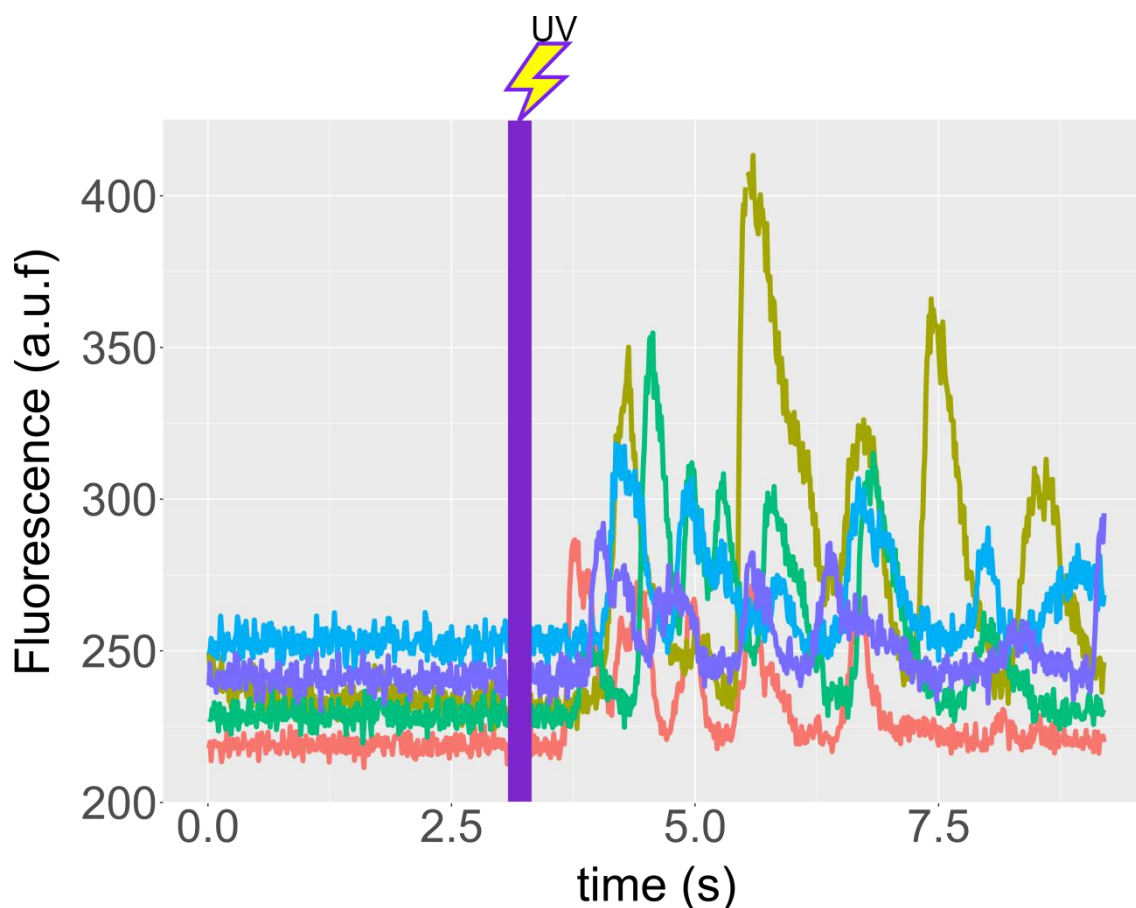
885 **Figure 5. *S. purpuratus* spermatozoa selectively experience chemotaxis towards**  
 886 **speract gradients.** Chemotactic behavior quantified using the linear equation  
 887 chemotaxis index (*LECI*) before (a), as control experiment, and after exposure to either  
 888 *f1, f2, f3, f4* or *f5* speract gradients (b, c). The color scale indicates the mean *LECI* value  
 889 calculated from tens of *S. purpuratus* spermatozoa located in either R1, R2, R3, or R4  
 890 regions prior speract photo-release (3 s after UV light irradiation (b), or 6 s after UV  
 891 light exposure (c)). Positive *LECI*s (shown in red) indicate movement towards the  
 892 chemoattractant source. Note that spermatozoa that were in R3 and R4 distal regions  
 893 prior speract gradient exposure experience chemotaxis only in response to *f2, f3*, and *f5*  
 894 speract gradients (b, c). Numerals indicate the number of spermatozoa analyzed in each  
 895 experimental condition. \*Statistical significance,  $p < 0.05$ ; Student's t-test.



896

897 **Figure 6. The slope of the speract gradient generates a frequency-locking**  
 898 **phenomenon between the stimulus function and the internal  $\text{Ca}^{2+}$  oscillator**  
 899 **triggered by speract. a.** Maximum relative slopes ( $\xi_{\max}$ ) experienced by *S. purpuratus*  
 900 (Sp) when exposed to  $f1$ ,  $f2$ ,  $f3$ ,  $f4$ ,  $f5$  speract gradients. The maximum relative slopes  
 901 experienced by *L. pictus* spermatozoa (Lp) towards  $f4$  experimental regime are also  
 902 shown. Note that  $\xi_{\max}$  for  $f2$ ,  $f3$ , and  $f5$ , are up to 2-3 times greater than in  $f4$ , regardless  
 903 of the species. **b.** Arnold's tongue indicating the difference in intrinsic frequency of the  
 904 internal  $\text{Ca}^{2+}$  oscillator of *S. purpuratus* spermatozoa, just before and after the speract  
 905 gradient exposure. **c.** Phase difference between the time derivative of the stimulus  
 906 function and the internal  $\text{Ca}^{2+}$  oscillator of *S. purpuratus* spermatozoa, obtained by  
 907 computing the cross-correlation function between both time series (**Figure 6 - figure**

908 **supplement 2). d.** Phase difference between the time derivative of the stimulus function  
909 and the internal  $\text{Ca}^{2+}$  oscillator of *S. purpuratus* spermatozoa expressed in temporal  
910 delays. **b-d.** Gray points represent the collapsed data of all *f1*, *f2*, *f3*, *f4*, *f5* experimental  
911 regimes. Red, black and blue points indicate chemotactic spermatozoa ( $\text{LECI} > 1$ ),  
912 located in R3, and R4 regions just before the speract gradient is established under *f2*, *f3*  
913 and *f5* experimental regimes, respectively. Magenta lines represent the transition  
914 boundary ( $\gamma_{\min} = \overline{\zeta_{\max}^*} \sim 2.7 \times 10^{-4}$ ) below which synchrony is not observed, obtained  
915 from the theoretical estimates (black curves) of panels **c** and **d**. Green lines indicate  
916 confidence intervals.



917

918 **Figure 6 - figure supplement 1. Speract induces  $\text{Ca}^{2+}$  oscillations in immobilized *S.***

919 ***purpuratus* spermatozoa.** Spermatozoa were immobilized on cover slips coated with

920 poly-D-lysine (see **Materials and Methods**), and ASW containing 500 nM caged

921 speract added. Recordings were performed 3s before and during 6s after 0.2s of UV

922 irradiation. *f4* optical fiber was used for the UV light path, to generate the speract

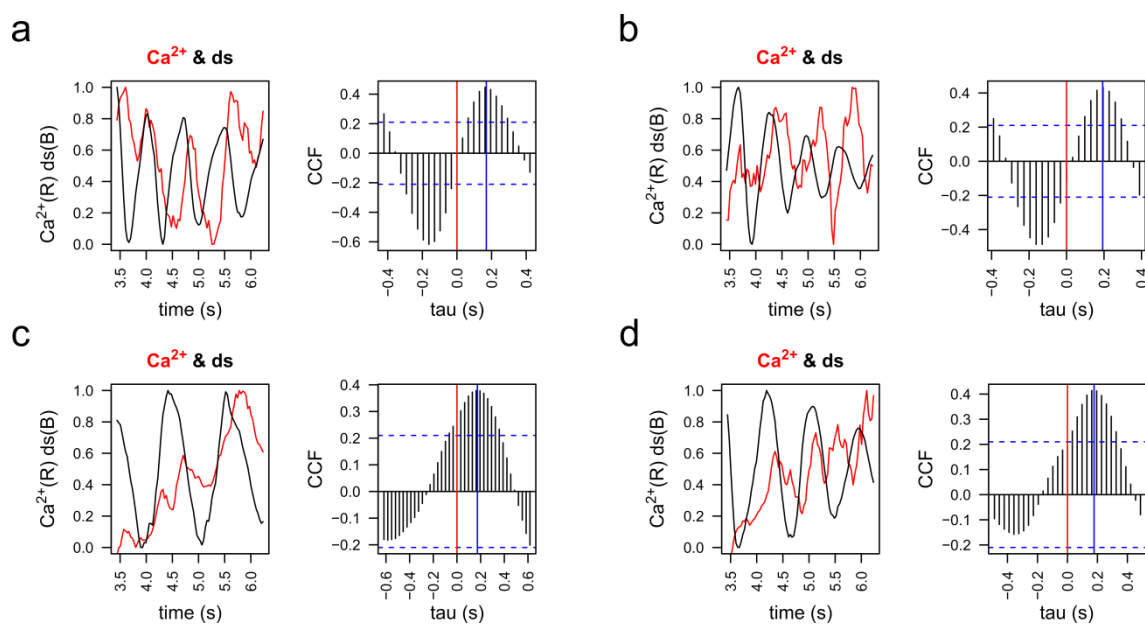
923 concentration gradient. The optical fiber was mounted on a “defocused” configuration

924 to minimize UV light heterogeneities producing photoactivated speract gradients. Time

925 traces indicate the  $[\text{Ca}^{2+}]_i$  of selected spermatozoa of **Movie 8**. Note that the photo-

926 release of speract induces a train of  $[\text{Ca}^{2+}]_i$  episodes in immobilized spermatozoa, hence

927 provides evidences for the presence of an internal  $\text{Ca}^{2+}$  oscillator triggered by speract.



928

929 **Figure 6 - figure supplement 2. Cross-correlation analysis of  $[Ca^{2+}]_i$  and stimulus**  
930 **function derivative (ds) signals.** Representative examples of  $[Ca^{2+}]_i$  and the derivate of  
931 the stimulus function (ds) were plotted and then analyzed by cross-correlation analysis  
932 (CCF). Examples of a pair of spermatozoa for the two principal chemotactic gradients  
933 ( $f_2$  and  $f_3$ ) are shown. **a, b.** Representative examples of two spermatozoa in  $f_2$  gradient.  
934 **c, d.** Representative examples of two spermatozoa in  $f_3$  gradient.

935 **Movies**

936 <https://www.dropbox.com/s/oe0mnc8j5r65l8s/Movie%201.avi?dl=0>

937 **Movie 1. Typical motility and  $\text{Ca}^{2+}$  responses of *S. purpuratus* spermatozoa**  
938 **towards *f2*-generated speract concentration gradient.** Spermatozoa swimming in  
939 artificial sea water containing 10 nM caged speract, 3 s before and 5 s after 200 ms UV  
940 irradiation. An optical fiber of 0.6 mm internal diameter was used for the UV light path  
941 to generate the speract concentration gradient. Real time: 31 frames  $\text{s}^{-1}$ , 40x /1.3NA oil-  
942 immersion objective. Note that spermatozoa located at R2, R3 and R4 regions prior  
943 speract exposure swim up the speract concentration gradient, towards the center of the  
944 imaging field. The pseudo-color scale represents the relative fluorescence of fluo-4, a  
945  $\text{Ca}^{2+}$  indicator, showing maximum (red) and minimum (blue) relative  $[\text{Ca}^{2+}]_i$ . Six *S.*  
946 *purpuratus* spermatozoa were manually tracked for visualization purposes. Scale bar of  
947 50  $\mu\text{m}$ .

948 <https://www.dropbox.com/s/v1h4kx6oqxc0f5l/Movie%202.avi?dl=0>

949 **Movie 2. Typical motility and  $\text{Ca}^{2+}$  responses of *S. purpuratus* spermatozoa**

950 **towards  $f_3$ -generated speract concentration gradient.** An optical fiber of 2 mm

951 internal diameter was used for the UV light path to generate the speract concentration

952 gradient. Other imaging conditions were set up as for Movie 1. Note that spermatozoa

953 located at R2, R3 and R4 regions prior to speract exposure swim up the speract

954 concentration gradient, towards the center of the imaging field. The pseudo-color scale

955 represents the relative fluorescence of fluo-4, a  $\text{Ca}^{2+}$  indicator, showing maximum (red)

956 and minimum (blue) relative  $[\text{Ca}^{2+}]_i$ . Six *S. purpuratus* spermatozoa were manually

957 tracked for visualization purposes. Scale bar of 50  $\mu\text{m}$ .

958 <https://www.dropbox.com/s/27v2i3ofda57fqs/Movie%203.avi?dl=0>

959 **Movie 3. Chemotaxis of *S. purpuratus* spermatozoa requires extracellular calcium.**

960 Spermatozoa swimming in artificial sea water with nominal calcium containing 10 nM  
961 caged speract 3 s before and 5 s after exposure to 200 ms UV light. Nominal calcium  
962 disrupts the electrochemical gradient required for  $\text{Ca}^{2+}$  influx, hence blocking the  
963 triggering of the internal  $\text{Ca}^{2+}$  oscillator by speract. The *f2* fiber (0.6 mm diameter) was  
964 used to uncage speract in this control. Other imaging conditions were set up as for  
965 Movie 1. Note that spermatozoa re-located after speract uncaging but they fail to  
966 experience the  $\text{Ca}^{2+}$ -driven motility alteration triggered by speract. As a consequence  
967 they fail to experience chemotaxis (compare with Movie 1). The pseudo-color scale  
968 represents the relative fluorescence of fluo-4, a  $\text{Ca}^{2+}$  indicator, showing maximum (red)  
969 and minimum (blue) relative  $[\text{Ca}^{2+}]_i$ . Six *S. purpuratus* spermatozoa were manually  
970 tracked for visualization purposes. Scale bar of 50  $\mu\text{m}$ .

971 <https://www.dropbox.com/s/vft4aiw96fpf3sy/Movie%204.avi?dl=0>

972 **Movie 4. Disrupting the K<sup>+</sup> electrochemical gradient blocks chemotaxis of *S.***  
973 ***purpuratus* spermatozoa.** Cells were swimming in artificial sea water containing 40  
974 mM of KCl, and 10 nM caged speract 3 s before and 5 s after exposure to 200 ms UV  
975 light. High K<sup>+</sup> in the ASW blocks the hyperpolarization required for opening Ca<sup>2+</sup>  
976 channels, and hence prevents the triggering of the internal Ca<sup>2+</sup> oscillator by speract  
977 exposure. The *f2* fiber (0.6 mm diameter) was used to uncage speract in this control.  
978 Other imaging conditions were set up as for Movie 1. Note that spermatozoa re-located  
979 after speract uncaging but they fail to experience the Ca<sup>2+</sup>-driven motility alteration  
980 triggered by speract, and thus they fail to experience chemotaxis (compare with Movie  
981 1). The pseudo-color scale represents the relative fluorescence of fluo-4, a Ca<sup>2+</sup>  
982 indicator, showing maximum (red) and minimum (blue) relative [Ca<sup>2+</sup>]<sub>i</sub>. Six *S.*  
983 *purpuratus* spermatozoa were manually tracked for visualization purposes. Scale bar of  
984 50 μm.

985 <https://www.dropbox.com/s/1317nmh1yw9juov/Movie%205.avi?dl=0>

986 **Movie 5. Typical motility and  $\text{Ca}^{2+}$  responses of *S. purpuratus* spermatozoa**  
987 **towards *fI*-generated speract concentration gradient.** An optical fiber of 0.2 mm  
988 internal diameter was used for the UV light path to generate the speract concentration  
989 gradient. Other imaging conditions were set up as for Movie 1. Note that some  
990 spermatozoa re-located after speract uncaging but they fail to experience chemotaxis  
991 (compare with Movie 1). The pseudo-color scale represents the relative fluorescence of  
992 fluo-4, a  $\text{Ca}^{2+}$  indicator, showing maximum (red) and minimum (blue) relative  $[\text{Ca}^{2+}]_i$ .  
993 Six *S. purpuratus* spermatozoa were manually tracked for visualization purposes. Scale  
994 bar of 50  $\mu\text{m}$ .

995 <https://www.dropbox.com/s/qvwnyysbij6iz3b/Movie%206.avi?dl=0>

996 **Movie 6. Typical motility and  $\text{Ca}^{2+}$  responses of *S. purpuratus* spermatozoa**  
997 **towards *f4*-generated speract concentration gradient.** An optical fiber of 4 mm  
998 internal diameter was used for the UV light path to generate the speract concentration  
999 gradient. Other imaging conditions were set up as for Movie 1. Note that spermatozoa  
1000 re-located after speract uncaging but they fail to experience chemotaxis (compare with  
1001 Movie 1). The pseudo-color scale represents the relative fluorescence of fluo-4, a  $\text{Ca}^{2+}$   
1002 indicator, showing maximum (red) and minimum (blue) relative  $[\text{Ca}^{2+}]_i$ . Six *S.*  
1003 *purpuratus* spermatozoa were manually tracked for visualization purposes. Scale bar of  
1004 50  $\mu\text{m}$ .

1005 <https://www.dropbox.com/s/o5o1e2jpmfitb1k/Movie%207.avi?dl=0>

1006 **Movie 7. Typical motility and  $\text{Ca}^{2+}$  responses of *S. purpuratus* spermatozoa**  
1007 **towards *f5*-generated speract concentration gradient.** An optical fiber of 4 mm  
1008 internal diameter was used for the UV light path to generate the speract concentration  
1009 gradient. Other imaging conditions were set up as for Movie 1. Note that spermatozoa  
1010 located at R2, R3 and R4 regions prior to speract exposure swim up the speract  
1011 concentration gradient, towards the center of the imaging field. The pseudo-color scale  
1012 represents the relative fluorescence of fluo-4, a  $\text{Ca}^{2+}$  indicator, showing maximum (red)  
1013 and minimum (blue) relative  $[\text{Ca}^{2+}]_i$ . Six *S. purpuratus* spermatozoa were manually  
1014 tracked for visualization purposes. Scale bar of 50  $\mu\text{m}$ .

1015

1016 <https://www.dropbox.com/s/dfug8i1ckj6nku/Movie%208.avi?dl=0>

1017 **Movie 8. Photo-release of caged speract induces  $\text{Ca}^{2+}$  oscillations in immobilized *S.***

1018 ***purpuratus* spermatozoa.** Spermatozoa were immobilized, by coating the cover slip

1019 with a thin layer of poly-D-lysine, in artificial sea water containing 500 nM caged

1020 speract, 3 s before and during 6 s after 0.2 s of UV irradiation. The *f4* optical fiber was

1021 used for the UV light path to generate the speract concentration gradient. The optical

1022 fiber was mounted on a “defocused” configuration to minimize the generation of UV

1023 light heterogeneities. 93 frames  $\text{s}^{-1}$ , 40x/1.3NA oil-immersion objective, 4x4 binning.

1024 The pseudo-color scale represents the relative fluorescence of fluo-4, a  $\text{Ca}^{2+}$  indicator,

1025 showing maximum (red) and minimum (blue) relative  $[\text{Ca}^{2+}]_i$ . The brightness and

1026 contrast scale was adjusted for better visualization of  $[\text{Ca}^{2+}]_i$  transients in the sperm

1027 flagella (as a consequence some heads look artificially oversaturated, however no

1028 fluorescence saturation was observed in the raw data).

1029

1030

1031        **References**

- 1032        2011. R: A Language and Environment for Statistical Computing. Vienna, Austria : the  
1033        R Foundation for Statistical Computing: R Development Core Team.
- 1034        AGUILERA, L. U., GALINDO, B. E., SANCHEZ, D. & SANTILLAN, M. 2012. What  
1035        is the core oscillator in the speract-activated pathway of the Strongylocentrotus  
1036        purpuratus sperm flagellum? *Biophys J*, 102, 2481-8.
- 1037        ALVAREZ, L., DAI, L., FRIEDRICH, B. M., KASHIKAR, N. D., GREGOR, I.,  
1038        PASCAL, R. & KAUPP, U. B. 2012. The rate of change in Ca(2+)  
1039        concentration controls sperm chemotaxis. *J Cell Biol*, 196, 653-63.
- 1040        AREF, H., BLAKE, J. R., BUDIŠIĆ, M., CARTWRIGHT, J. H. E., CLERCX, H. J. H.,  
1041        FEUDEL, U., GOLESTANIAN, R., GOUILLART, E., LE GUER, Y., VAN  
1042        HEIJST, G. F., KRASNOPOLSKAYA, T. S., MACKAY, R. S., MELESHKO,  
1043        V. V., METCALFE, G., MEZIĆ, I., DE MOURA, A. P. S., EL OMARI, K.,  
1044        PIRO, O., SPEETJENS, M. F. M., STURMAN, R., THIFFEAULT, J. L. &  
1045        TUVAL, I. 2014. Frontiers of chaotic advection. *Reviews of Modern Physics*,  
1046        1403, 61.
- 1047        BATCHELOR, G. K. 2006. Small-scale variation of convected quantities like  
1048        temperature in turbulent fluid Part 1. General discussion and the case of small  
1049        conductivity. *Journal of Fluid Mechanics*, 5, 113.
- 1050        BERG, H. C. & PURCELL, E. M. 1977. Physics of chemoreception. *Biophys J*, 20,  
1051        193-219.
- 1052        BOHMER, M., VAN, Q., WEYAND, I., HAGEN, V., BEYERMANN, M.,  
1053        MATSUMOTO, M., HOSHI, M., HILDEBRAND, E. & KAUPP, U. B. 2005.  
1054        Ca<sup>2+</sup> spikes in the flagellum control chemotactic behavior of sperm. *EMBO J*,  
1055        24, 2741-52.
- 1056        BROKAW, C. J. 1979. Calcium-induced asymmetrical beating of triton-  
1057        demembrated sea urchin sperm flagella. *J Cell Biol*, 82, 401-11.
- 1058        COOK, S. P., BROKAW, C. J., MULLER, C. H. & BABCOCK, D. F. 1994. Sperm  
1059        chemotaxis: egg peptides control cytosolic calcium to regulate flagellar  
1060        responses. *Dev Biol*, 165, 10-9.
- 1061        DARSZON, A., GUERRERO, A., GALINDO, B. E., NISHIGAKI, T. & WOOD, C. D.  
1062        2008. Sperm-activating peptides in the regulation of ion fluxes, signal  
1063        transduction and motility. *Int J Dev Biol*, 52, 595-606.
- 1064        DUSENBERY, D. B. 2011. *Living at micro scale: The unexpected physics of being  
1065        small*, Harvard University Press.
- 1066        ESPINAL, J., ALDANA, M., GUERRERO, A., WOOD, C., DARSZON, A. &  
1067        MARTINEZ-MEKLER, G. 2011. Discrete dynamics model for the speract-  
1068        activated Ca<sup>2+</sup> signaling network relevant to sperm motility. *PLoS One*, 6,  
1069        e22619.
- 1070        FRIEDRICH, B. M. & JÜLICHER, F. 2007. Chemotaxis of sperm cells. *Proc Natl  
1071        Acad Sci U S A*, 104, 13256-61.
- 1072        FRIEDRICH, B. M. & JÜLICHER, F. 2008. The stochastic dance of circling sperm  
1073        cells: sperm chemotaxis in the plane. *New Journal of Physics*, 10, 123025.
- 1074        FRIEDRICH, B. M. & JÜLICHER, F. 2009. Steering chiral swimmers along noisy  
1075        helical paths. *Phys Rev Lett*, 103, 068102.
- 1076        GARCES, Y., GUERRERO, A., HIDALGO, P., LOPEZ, R. E., WOOD, C. D.,  
1077        GONZALEZ, R. A. & RENDON-MANCHA, J. M. 2016. Automatic detection  
1078        and measurement of viral replication compartments by ellipse adjustment. *Sci  
1079        Rep*, 6, 36505.

- 1080 GUERRERO, A., NISHIGAKI, T., CARNEIRO, J., YOSHIRO, T., WOOD, C. D. &  
1081 DARSZON, A. 2010a. Tuning sperm chemotaxis by calcium burst timing. *Dev*  
1082 *Biol*, 344, 52-65.
- 1083 GUERRERO, A., WOOD, C. D., NISHIGAKI, T., CARNEIRO, J. & DARSZON, A.  
1084 2010b. Tuning sperm chemotaxis. *Biochem Soc Trans*, 38, 1270-4.
- 1085 HANSBROUGH, J. R. & GARBERS, D. L. 1981. Speract. Purification and  
1086 characterization of a peptide associated with eggs that activates spermatozoa. *J*  
1087 *Biol Chem*, 256, 1447-52.
- 1088 HUSSAIN, Y. H., SADILEK, M., SALAD, S., ZIMMER, R. K. & RIFFELL, J. A.  
1089 2017. Individual female differences in chemoattractant production change the  
1090 scale of sea urchin gamete interactions. *Dev Biol*, 422, 186-197.
- 1091 JIKELI, J. F., ALVAREZ, L., FRIEDRICH, B. M., WILSON, L. G., PASCAL, R.,  
1092 COLIN, R., PICHLO, M., RENNHACK, A., BRENKER, C. & KAUPP, U. B.  
1093 2015. Sperm navigation along helical paths in 3D chemoattractant landscapes.  
1094 *Nat Commun*, 6, 7985.
- 1095 JIMÉNEZ, J. 1997. Oceanic turbulence at millimeter scales. *Scientia Marina*, 61, 47-56.
- 1096 KASHIKAR, N. D., ALVAREZ, L., SEIFERT, R., GREGOR, I., JACKLE, O.,  
1097 BEYERMANN, M., KRAUSE, E. & KAUPP, U. B. 2012. Temporal sampling,  
1098 resetting, and adaptation orchestrate gradient sensing in sperm. *J Cell Biol*, 198,  
1099 1075-91.
- 1100 KAUPP, U. B. 2012. 100 years of sperm chemotaxis. *J Gen Physiol*, 140, 583-6.
- 1101 KAUPP, U. B., KASHIKAR, N. D. & WEYAND, I. 2008. Mechanisms of sperm  
1102 chemotaxis. *Annu Rev Physiol*, 70, 93-117.
- 1103 KAUPP, U. B., SOLZIN, J., HILDEBRAND, E., BROWN, J. E., HELBIG, A.,  
1104 HAGEN, V., BEYERMANN, M., PAMPALONI, F. & WEYAND, I. 2003. The  
1105 signal flow and motor response controlling chemotaxis of sea urchin sperm. *Nat*  
1106 *Cell Biol*, 5, 109-17.
- 1107 LAKOWICZ, J. R. 2006. *Principles of Fluorescence Spectroscopy*, Springer US.
- 1108 LILLIE, F. R. 1913. The mechanism of fertilization. *Science*, 38, 524-528.
- 1109 LOTTERHOS, K. E. L., D. R. 2010. *Gamete release and spawning behavior in*  
1110 *broadcast spawning marine invertebrates*, New York, NY, Oxford University  
1111 Press.
- 1112 MAUPETIT, J., DERREUMAUX, P. & TUFFERY, P. 2009. PEP-FOLD: an online  
1113 resource for de novo peptide structure prediction. *Nucleic Acids Res*, 37, W498-  
1114 503.
- 1115 MAUPETIT, J., DERREUMAUX, P. & TUFFERY, P. 2010. A fast method for large-  
1116 scale de novo peptide and miniprotein structure prediction. *J Comput Chem*, 31,  
1117 726-38.
- 1118 MEAD, K. S. & DENNY, M. W. 1995. The effects of hydrodynamic shear stress on  
1119 fertilization and early development of the purple sea urchin *Strongylocentrotus*  
1120 *purpuratus*. *Biol Bull*, 188, 46-56.
- 1121 MEIJERING, E., DZYUBACHYK, O. & SMAL, I. 2012. Methods for cell and particle  
1122 tracking. *Methods Enzymol*, 504, 183-200.
- 1123 MILLER, R. L. 1985. Sperm Chemo-Orientation in the Metazoa. In: METZ, C. B. &  
1124 MONROY, A. (eds.) *Biology of Fertilization*. New York: Academic Press.
- 1125 NISHIGAKI, T. & DARSZON, A. 2000. Real-time measurements of the interactions  
1126 between fluorescent speract and its sperm receptor. *Dev Biol*, 223, 17-26.
- 1127 NISHIGAKI, T., ZAMUDIO, F. Z., POSSANI, L. D. & DARSZON, A. 2001. Time-  
1128 resolved sperm responses to an egg peptide measured by stopped-flow  
1129 fluorometry. *Biochem Biophys Res Commun*, 284, 531-5.

- 1130 PETERSEN, E. F., GODDARD, T. D., HUANG, C. C., COUCH, G. S.,  
1131 GREENBLATT, D. M., MENG, E. C. & FERRIN, T. E. 2004. UCSF Chimera--  
1132 a visualization system for exploratory research and analysis. *J Comput Chem*,  
1133 25, 1605-12.
- 1134 PFEFFER, W. 1884. Locomotorische Richtungsbewegungen durch chemische Reize. In  
1135 *Untersuchungen aus dem botanischen Institut zu Tübingen*, 1, 363-482.
- 1136 PICHLO, M., BUNGERT-PLUMKE, S., WEYAND, I., SEIFERT, R., BONIGK, W.,  
1137 STRUNKER, T., KASHIKAR, N. D., GOODWIN, N., MULLER, A., PELZER,  
1138 P., VAN, Q., ENDERLEIN, J., KLEMM, C., KRAUSE, E., TROTSCHER, C.,  
1139 POETSCH, A., KREMMER, E., KAUPP, U. B., KORSCHEN, H. G. &  
1140 COLLIENNE, U. 2014. High density and ligand affinity confer ultrasensitive  
1141 signal detection by a guanylyl cyclase chemoreceptor. *J Cell Biol*, 206, 541-57.
- 1142 PIKOVSKY, A., ROSENBLUM, M. & KURTHS, J. 2001. *Synchronization. A*  
1143 *Universal Concept in Nonlinear Sciences*, Cambridge University Press; 1  
1144 edition.
- 1145 RIFFELL, J. A. & ZIMMER, R. K. 2007. Sex and flow: the consequences of fluid shear  
1146 for sperm-egg interactions. *J Exp Biol*, 210, 3644-60.
- 1147 SCHNEIDER, C. A., RASBAND, W. S. & ELICEIRI, K. W. 2012. NIH Image to  
1148 ImageJ: 25 years of image analysis. *Nat Methods*, 9, 671-5.
- 1149 SHIBA, K., BABA, S. A., INOUE, T. & YOSHIDA, M. 2008. Ca<sup>2+</sup> bursts occur  
1150 around a local minimal concentration of attractant and trigger sperm chemotactic  
1151 response. *Proc Natl Acad Sci U S A*, 105, 19312-7.
- 1152 SHIMOMURA, H. & GARBERS, D. L. 1986. Differential effects of resact analogues  
1153 on sperm respiration rates and cyclic nucleotide concentrations. *Biochemistry*,  
1154 25, 3405-10.
- 1155 SMITH, A. C. & GARBERS, D. L. 1983. The binding of an <sup>125</sup>I-speract analogue to  
1156 spermatozoa. In: LENNON, D. L., STRATMAN, F. W. & ZAHLTEN, R. N.,  
1157 eds. *Biochemistry of Metabolic Processes*, 1982 Madison, Wisconsin, U.S.A.  
1158 Amsterdam, New York, U.S.A.: Elsevier, 496.
- 1159 STRUNKER, T., ALVAREZ, L. & KAUPP, U. B. 2015. At the physical limit -  
1160 chemosensation in sperm. *Curr Opin Neurobiol*, 34, 110-6.
- 1161 SUZUKI, N. 1995. Structure, function and biosynthesis of sperm-activating peptides  
1162 and fucose sulfate glycoconjugate in the extracellular coat of sea urchin eggs.  
1163 *Zoolog Sci*, 12, 13-27.
- 1164 TATSU, Y., NISHIGAKI, T., DARSZON, A. & YUMOTO, N. 2002. A caged sperm-  
1165 activating peptide that has a photocleavable protecting group on the backbone  
1166 amide. *FEBS Lett*, 525, 20-4.
- 1167 THEVENET, P., SHEN, Y., MAUPETIT, J., GUYON, F., DERREUMAUX, P. &  
1168 TUFFERY, P. 2012. PEP-FOLD: an updated de novo structure prediction server  
1169 for both linear and disulfide bonded cyclic peptides. *Nucleic Acids Res*, 40,  
1170 W288-93.
- 1171 THORPE, S. A. 2007. *An Introduction to Ocean Turbulence*, Cambridge University  
1172 Press.
- 1173 VERGASSOLA, M., VILLERMAUX, E. & SHRAIMAN, B. I. 2007. 'Infotaxis' as a  
1174 strategy for searching without gradients. *Nature*, 445, 406-9.
- 1175 WOOD, C. D., DARSZON, A. & WHITAKER, M. 2003. Speract induces calcium  
1176 oscillations in the sperm tail. *J Cell Biol*, 161, 89-101.
- 1177 WOOD, C. D., GUERRERO, A., PRIEGO-ESPINOSA, D. A., MARTÍNEZ-MEKLER,  
1178 G., CARNEIRO, J. & DARSZON, A. 2015. Sea Urchin Sperm Chemotaxis. In:

- 1179 COSSON, J. J. (ed.) *Flagellar Mechanics and Sperm Guidance*. Czech  
1180 Republic: Bentham Science Publishers.
- 1181 WOOD, C. D., NISHIGAKI, T., FURUTA, T., BABA, S. A. & DARSZON, A. 2005.  
1182 Real-time analysis of the role of Ca(2+) in flagellar movement and motility in  
1183 single sea urchin sperm. *J Cell Biol*, 169, 725-31.
- 1184 WOOD, C. D., NISHIGAKI, T., TATSU, Y., YUMOTO, N., BABA, S. A.,  
1185 WHITAKER, M. & DARSZON, A. 2007. Altering the speract-induced ion  
1186 permeability changes that generate flagellar Ca<sup>2+</sup> spikes regulates their kinetics  
1187 and sea urchin sperm motility. *Dev Biol*, 306, 525-37.
- 1188 YOSHIDA, M., MURATA, M., INABA, K. & MORISAWA, M. 2002. A  
1189 chemoattractant for ascidian spermatozoa is a sulfated steroid. *Proc Natl Acad  
1190 Sci U S A*, 99, 14831-6.
- 1191 ZIMMER, R. K. & RIFFELL, J. A. 2011. Sperm chemotaxis, fluid shear, and the  
1192 evolution of sexual reproduction. *Proc Natl Acad Sci U S A*, 108, 13200-5.  
1193